Analysis of the Temporal and Spacial Signal Propagation of a Triple GEM Detector

von

Anna Becker

Bachelorarbeit in Physik

vorgelegt der
Fakultät für Mathematik, Informatik und
Naturwissenschaften der RWTH Aachen

angefertigt im
III. Physikalischen Institut A

bei
Prof. Dr. Thomas Hebbeker

Zweitgutachter
Prof. Dr. Christopher Wiebusch

Mai 2018

Zentrales Prüfungsamt/Central Examination Office

Eidesstattliche Versicherung
Statutory Declaration in Lieu of an Oath

_____ _____

Name, Vorname/Last Name, First Name

Matrikelnummer (freiwillige Angabe)
Matriculation No. (optional)

Ich versichere hiermit an Eides Statt, dass ich die vorliegende Arbeit/Bachelorarbeit/ Masterarbeit* mit dem Titel
I hereby declare in lieu of an oath that I have completed the present paper/Bachelor thesis/Master thesis* entitled

_____

_____

_____

selbstständig und ohne unzulässige fremde Hilfe (insbes. akademisches Ghostwriting) erbracht habe. Ich habe keine anderen als die angegebenen Quellen und Hilfsmittel benutzt. Für den Fall, dass die Arbeit zusätzlich auf einem Datenträger eingereicht wird, erkläre ich, dass die schriftliche und die elektronische Form vollständig übereinstimmen. Die Arbeit hat in gleicher oder ähnlicher Form noch keiner Prüfungsbehörde vorgelegen.
independently and without illegitimate assistance from third parties (such as academic ghostwriters). I have used no other than the specified sources and aids. In case that the thesis is additionally submitted in an electronic format, I declare that the written and electronic versions are fully identical. The thesis has not been submitted to any examination body in this, or similar, form.

_____ _____

Ort, Datum/City, Date

Unterschrift/Signature

*Nichtzutreffendes bitte streichen

*Please delete as appropriate

Belehrung:
Official Notification:

§ 156 StGB: Falsche Versicherung an Eides Statt
Wer vor einer zur Abnahme einer Versicherung an Eides Statt zuständigen Behörde eine solche Versicherung falsch abgibt oder unter Berufung auf eine solche Versicherung falsch aussagt, wird mit Freiheitsstrafe bis zu drei Jahren oder mit Geldstrafe bestraft.
Para. 156 StGB (German Criminal Code): False Statutory Declarations
Whoever before a public authority competent to administer statutory declarations falsely makes such a declaration or falsely testifies while referring to such a declaration shall be liable to imprisonment not exceeding three years or a fine.
§ 161 StGB: Fahrlässiger Falscheid; fahrlässige falsche Versicherung an Eides Statt
(1) Wenn eine der in den §§ 154 bis 156 bezeichneten Handlungen aus Fahrlässigkeit begangen worden ist, so tritt Freiheitsstrafe bis zu einem Jahr oder Geldstrafe ein.
(2) Straflosigkeit tritt ein, wenn der Täter die falsche Angabe rechtzeitig berichtigt. Die Vorschriften des § 158 Abs. 2 und 3 gelten entsprechend.
Para. 161 StGB (German Criminal Code): False Statutory Declarations Due to Negligence
(1) If a person commits one of the offences listed in sections 154 through 156 negligently the penalty shall be imprisonment not exceeding one year or a fine.
(2) The offender shall be exempt from liability if he or she corrects their false testimony in time. The provisions of section 158 (2) and (3) shall apply accordingly.

Die vorstehende Belehrung habe ich zur Kenntnis genommen:
I have read and understood the above official notification:

_____ _____

Ort, Datum/City, Date

Unterschrift/Signature

Contents

1 Introduction

Since the beginning of the 20th century, particle physics exists in the way we know it today. After the discovery of electron (1897), proton (1919), neutron (1932) and positron (1932) Carl D. Anderson and Seth Neddermeyer identified a new particle in 1936 by cloud chamber experiments. They measured the energy loss of cosmic rays as they passed through a platinum plate in a cloud chamber. As a result, Anderson and Neddermeyer concluded that the cause must be a particle heavier than the electron. Since 1947 it has been known that the particle measured by Anderson and Neddermeyer was a previously unknown particle, the muon. Discoveries like this motivates particle physicists all over the world to search for new particles in order to better understand the structure of matter and the universe as a whole. For this reason, new and better detector concepts have been and are still being developed.

The history of particle detectors starts about 15 years before the first muon detection with the creation of the Wilson Cloud Chamber in 1911 by Charles T. R. Wilson. Only one year later Hans Geiger developed the famous Geiger counter named after him. These first detectors were only able to qualitatively measure the amount of ionizing radiation. But the technique for detecting electromagnetically interacting particles has been further improved: On the one hand, the Wilson cloud chamber has been further developed into triggerable diffusion cloud chambers (triggerable chamber: Patrick M. S. Blackett & Guiseppe P. S. Occhiallini 1932; diffusion chamber: Alexander Langsdorf 1936). The development of this type of detectors ended with the invention of the bubble chamber by Donald A. Blaser in 1952 which were used until the 1980s. These trace detectors made it possible to observe a higher rate of particle traces over a longer period of time than before. Nowadays these trace detectors are solid state detectors which are out of the scope of this thesis.
On the other hand the original Geiger counter was also further upgraded to the Geiger-Müller counter tube in 1928, which enables the detection of ionizing particles without differentiation of particle type and energy. With the development of the proportional counter, a counter tube similar to the Geiger-Müller counter but working at a lower counter tube voltage, one was also able to measure the energy of particles. The functional principle of these early gas detectors is easy but elementary: between a thin wire, the anode, and a cathode an electric field is generated, while the surrounding area is filled with the counting gas. When a particle passes the detector it ionizes some gas atoms; depending on the electric field and the geometry of the counter a flow of positively charged ions to the cathode and electrons to the anode is induced causing an measurable electric signal at the counting wire.
Many new methods for particle detection based on this basic principal were created in the following years, such as the the drift chamber which Georges Charpack developed in 1968. Especially the technology of gas detectors has been further developed into detectors with ever increasing energy, momentum and spatial resolution. One example are the micropattern gas detectors (MPGD) which were established in the 1980s. MPGDs are a type of detectors which utilizes microscopic structures to achieve charge amplification together with fast ion collection, thus providing improved performance at high particle rates. In particular these detectors allow a better spatial resolution, a higher rate and a higher efficiency, so they are performing much better than wire chambers. Mainly there are two different types of MPGDs: micro mesh gas detectors (MicroMEGAS) and gas electron multipliers (GEM). The latter are the type of detector used in this thesis and so their mode of functioning will be introduced below and in more detail in chapter 2 [5] and [6].

Nowadays GEMs are widely used detectors for the detection of muons. They were developed in 1997 by a Gas Detector Development Group at CERN and they are still in use

in various experiments worldwide (COMPASS, PHENIX, LHC-b, etc.). The basic concept of a gas detector described above remains unchanged, but especially its geometry is modified and refined. Similar to an ionization chamber, a high voltage of some kV is applied between anode, the so-called readout board, and cathode, the drift board. Between these is a thin so-called GEM-foil; it is the centrepiece of the GEM detector. The foil consists of a polyimide that is clad on both sides with copper. There is a potential difference of several hundred Volts between the copper layers. Thus it is part of the voltage gradient between drift cathode and readout plane. In addition, the foil contains a large number of μm-sized holes that make it permeable to ions and electrons. Three such foils are integrated with a distance of a few millimetres between anode and cathode to build a triple-GEM chamber (see ch. 2).

In this thesis the temporal and spacial signal propagation of a triple-GEM chamber under variation of different parameters is analysed. For the experiments an X-ray source is used. Both, X-rays and muons, ionize the gas molecules while travelling through the volume of the detector. To make frequent and easily reproducible measurements it is simpler to use an X-ray source, because cosmic muons are not uniformly distributed or present at a high frequency.
In the various measurements, both the high voltage applied to the chamber is varied by several hundred volts and the signal amplification at the measuring electronics is changed (see ch. 2). In order to be able to observe even small signals, the measured data are recorded without a threshold as a preliminary filter, called raw data mode, and then later analysed with a self-programmed ”unpacker”. This program is also a part of this thesis (see ch. 3).

This thesis is structured as follows: First, in chapter 2 ”Experimental Set up”, the GEM chamber and the measuring electronics as well as the test settings are described in detail. The chapter 3 ”Analysis” starts with the structure of the ”unpacker” program. The focus here is particularly on how the code is structured in relation to reading the measurement data from the SRS data format and how information about the signal propagation is obtained. Then the analysis of the measured data using the unpacker and its results are displayed. Followed by the last chapter 4 ”Summary and Conclusion”, which summarizes and discusses the results of the analysis, draws conclusions from it and gives an outlook on further questions in connection with the results of this work.

2 Experimental Set up

The following chapter contains an overview of the experimental set up used for the characterization of a GEM chamber. First the design and function of the GEM chambers and then the measuring electronics with focus on the Scalable Readout System (SRS or SR-System) are presented and briefly discussed. Finally the entire test setup is described.

2.1 GEM Chambers

The schematic construction of a triple GEM chamber is shown in fig. 2.1. It consists of a readout board (anode) and a drift board (cathode). The three GEM foils are located between them. Drift gap, transfer gap 1 & 2 and induction gap have a spacing of 3/1/2/1 mm. Between the readout board and the drift board a high voltage (HV) up to 3300 V is applied. The GEM foils are connected via resistors to the voltage potential between anode and cathode (see fig. 2.2). The one between the drift board and the first GEM foil has the highest resistance with $\sim$1.100 MΩ. Between the foils 1 & 2 a resistor of $\sim$450 kΩ is used, between 2 & 3 it is $\sim$850 kΩ. Between GEM foil 3 and the readout board there is a resistance of $\sim$600 kΩ. The top and the bottom of the foils are connected via $\sim$550 kΩ resistors. So the potential increases stepwise between the GEM foils.

Drift and readout board are made of fibreglass (FR4) surrounded by copper. There are in total 3072 readout strips covering the entire readout plane. It is divided into 24 sectors (see fig. 2.3) with 128 strips each. Because of the trapezoidal design of the chamber, the shape of the strips is truly radial. They have a width of 230 μrad and are placed about 463 μrad apart. The vertex of the strips is aligned in the expected direction of the ionizing particles. The strips are connected to the inputs of a front-end Application-Specific Integrated Circuit (ASIC) by a connector outside of the readout board. The 128 strips of every sector are assigned to an Analogue Pipeline Voltage-mode (APV) chip. Each APV consists of 128 analogue input channels, so readout strip and channels are linked one by one. The channels are assigned to some preamplifiers and divided into two groups: even and odd numbered channels. Each of the 3072 APV channels records an adjustable number of time bins with a duration of 25 ns. This will be relevant for programming the unpacker (see ch. 3). In total there are 24 APVs located on the readout board, one per sector. They are grouped in 12 master- and slave-APV pairs (see fig. 2.5). The master-APVs are arranged at the edge of the chamber for easy connection. Overall, an efficiency of minimum 97%, an angular resolution of better than than 300 μrad and a timing resolution of better than 10 ns can be achieved with a single triple GEM detector.

The GEM foils, made of an insulating polyamide, are coated on both sides with copper to make the top and the bottom of them conductive. They have a high density of microscopic holes, which make the foils permeable for drifting electrons and ions (see fig. 2.4, left). The holes have the shape of two superimposed truncated cones, so that the radius in the middle of the hole is smaller than that on the surface of the foil. The small distance creates an electric field strength up to $\sim$80 kV/cm in the middle of the hole. This is represented in fig. 2.4, right. This high electric field creates a high amplification, that makes the measurement of small signals possible.

The chamber is filled with an Ar/CO_2 mixture in a ratio of 70:30. The nominal operation gas flow is approximately one chamber volume per hour. If an ionizing particle hits the detector volume (schematically shown in fig. 2.1), some gas molecules are ionized in the drift gap.

The free electrons drift along the electric field lines in the direction of the anode. On the way to the readout plane they pass the three GEM foils and the transfer gaps between them. Especially in the holes the drifting electrons are strongly accelerated in the direction of the anode, due to of the high field strength inside the holes. The electrons can reach velocities of about $(7-8)\,\mathrm{cm}/\mu\mathrm{s}$. When they are colliding with gas atoms, the atoms get ionized and more free electrons are generated. When these generated electrons get accelerated in holes of the next GEM foil, they will ionize more gas atoms. Thus the electrons trigger again an electron shower in the holes. The ions, which are less accelerated by their size, drift to the cathode. So one can say the more acceleration the electrons experience, the more the signal of an incoming particle is amplified. When the electron shower reaches the readout board, a measurable voltage pulse is generated in neighbouring strips.

The technical information about the GEM chambers given in this subsection are taken from [2].

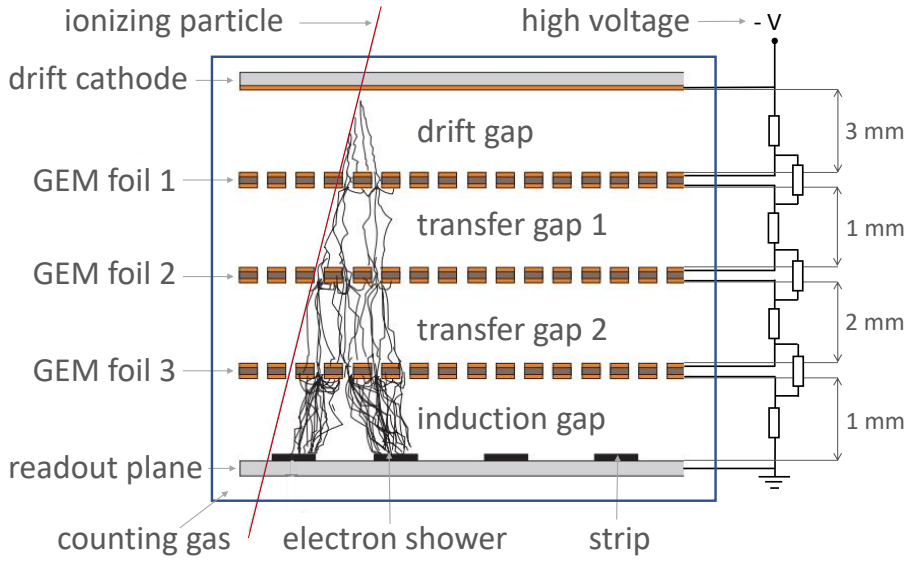

Figure 2.1: Schematic view of the construction of a triple GEM chamber and the schematic electron shower generation caused by an ionizing particle passing the detector. The HV divider is shown in fig. 2.2 in more detail. ([2] modified)

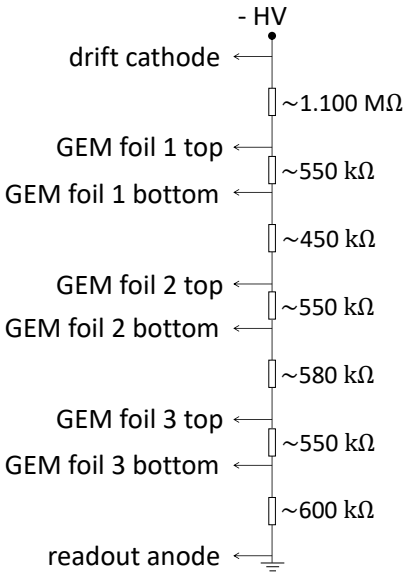

Figure 2.2: Schematic view of the voltage divider between drift board, GEM foils and readout board with the individual resistances. The total resistance is about 4400 MΩ. Additional a HV-filter with about 5 Ω is applied. So a typical voltage of 3300 V causes a current of 627 μA

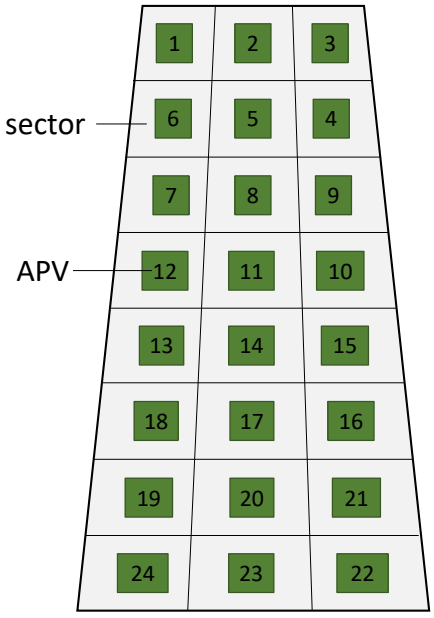

Figure 2.3: Schematic depiction of the trapezoidal design of a GEM chamber with marked sectors and a numbered APV on each

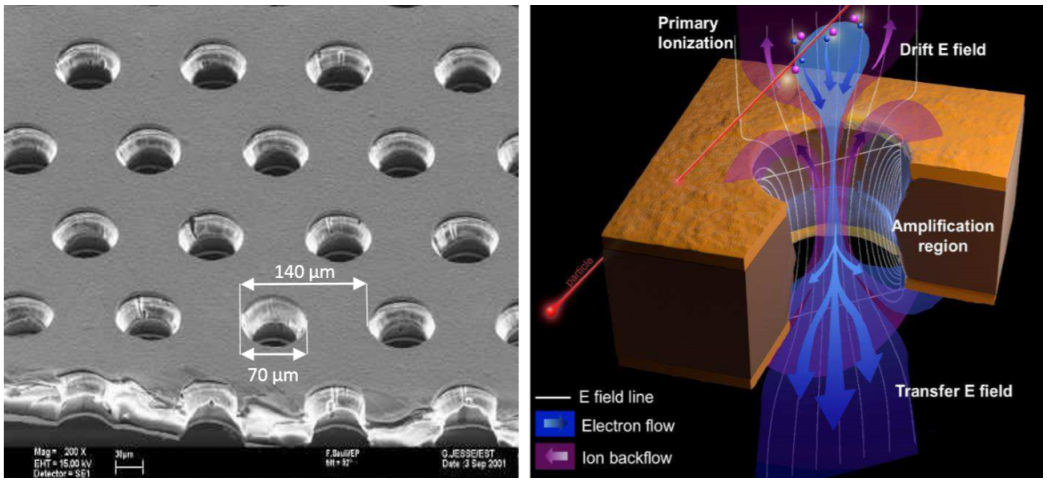

Figure 2.4: Left: Scanning Electron Microscope (SEM) picture of a GEM foil showing the hexagonal pattern of the GEM holes.
Right: Schematic view of the electric field lines (white), electron flow (blue), and ion flow (purple) through a GEM hole [2]

2.2 SR-System

The SR-System consists of two Analogue-to-Digital-Converter (ADC) cards and two Front End Controllers (FEC1 & FEC2) connected to them. The ADCs are connected to the 12 master APVs on the detector via HDMI cable. The mapping of this connection is shown in fig. 2.5. This is not relevant for the function of the detector, but it is important for the assignment of the measurement data to the APVs when programming the unpacker (see ch. 3). The FECs are linked to external triggers and the measurement PC. It hosts control system and storage.

2.2.1 SRS Data Format

The raw data transmitted by the APVs contain digital information in the form of the APV header (e.g. the channel info) and analogue measurement data. In the following this both is called the APV layer (see fig. 2.7). Digital and analogue data are communicated via the same "voltage line" by means of voltage drops, so the signals are falling in raw data. Therefore, the data will be inverted in the analysis (see fig. 2.6). One can see the APVs transmitting synchronization pulses before, after and between measurement data packages. A data package contains all the information that a single APV has measured, i.e. data from 128 strips with an adjusted number of time bins each. This results in a data structure of a single event as shown in fig. 2.6. An event is defined as all the in time bins measured analogue data[1] between two external trigger signal. The synchronization pulses are not synchronized with external triggers, so the length of the APV header varies between events. This requires a search in the "unpacker" for the beginning of the measurement data (see ch. 3). It should be noted, that the APVs are grouped into two parts: the ones connected to FEC 1 and the others to FEC 2. So there are two APV layers for each event.

The information (digital and analogue mixed) from the APVs are sent to the SR-System which is running in "Raw data mode (ADC mode)" for all measurements. It converts the incoming analogue data of the APVs into digital data, allows the setting of e.g. trigger and gain and adds a *FEC header* with information about e.g. trigger counter or data length to the *APV layer*. On the basis of the sync pulses in the *APV layer* the FEC is able to insert the header at the right position. The *FEC header* has a fixed length and contains information about data acquisition (DAQ) and header information e.g. the data source. Moreover information about the length of the *FEC header* is appended. This is called the *FEC layer* (see fig. 2.7). The communication between the FECs and the measurement PC operates by using a User Datagram Protocol (UDP), a network protocol. So a *UDP header* is also attached to the *FEC layer*. Thus the overall data format of a single event looks like the following (see also fig. 2.7): each event consists of its own *UDP layer*. The *UDP layer* consists of header information like the frame counter and the *FEC layer*. This consists of a *FEC header* and the *APV layer*. The structure of *APV layer* is described above. The information presented in this chapter about the SRS was taken from [3] and [4].

[1] The time lag after an external trigger signals is clearly longer than the measurement time of 25 ns times the adjusted number of time bins.

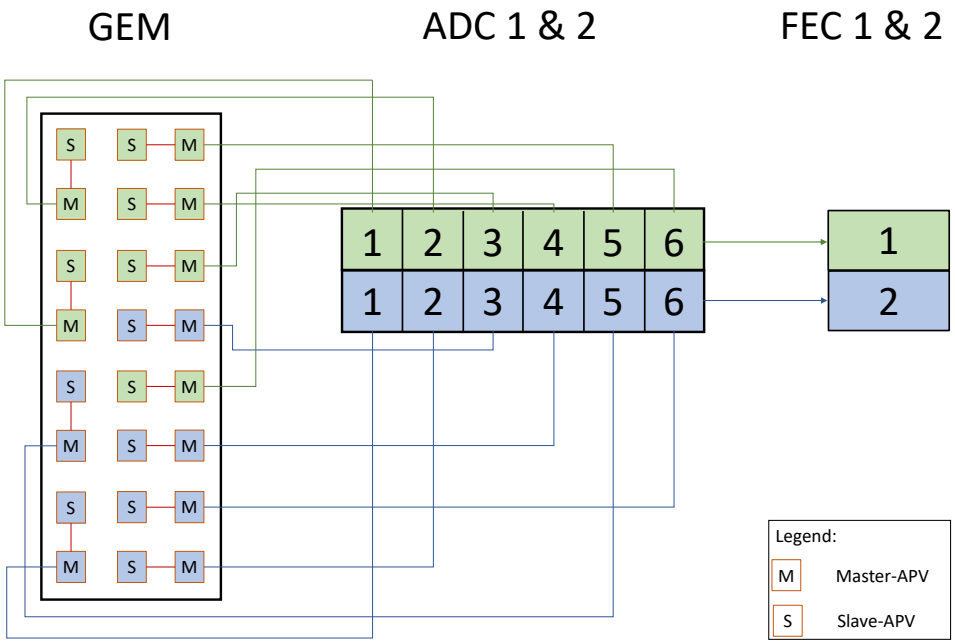

Figure 2.5: Schematic view of the connection from the GEM chamber to the SR-System (ADCs and FECs).

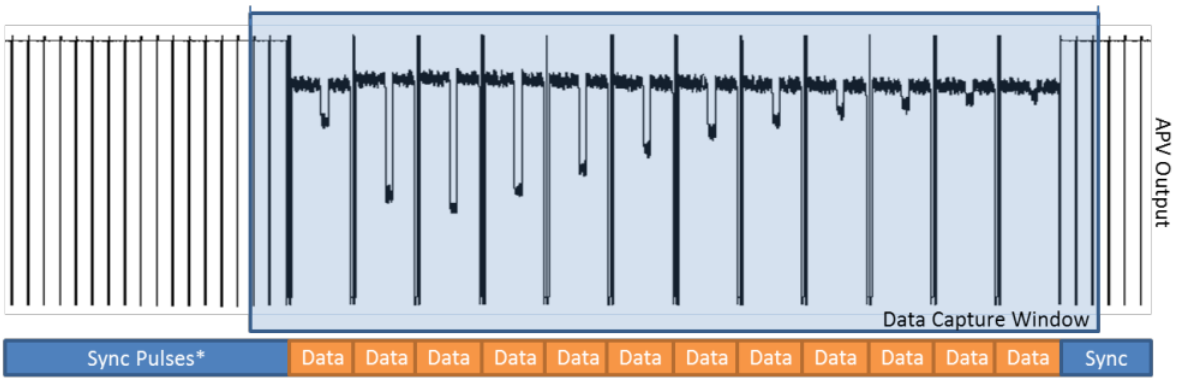

Figure 2.6: Schematic view of of the APV rawdata acquisition with sync pulses, which are not synchronized with the external triggers, so the position of the data could change inside the capture window [4].

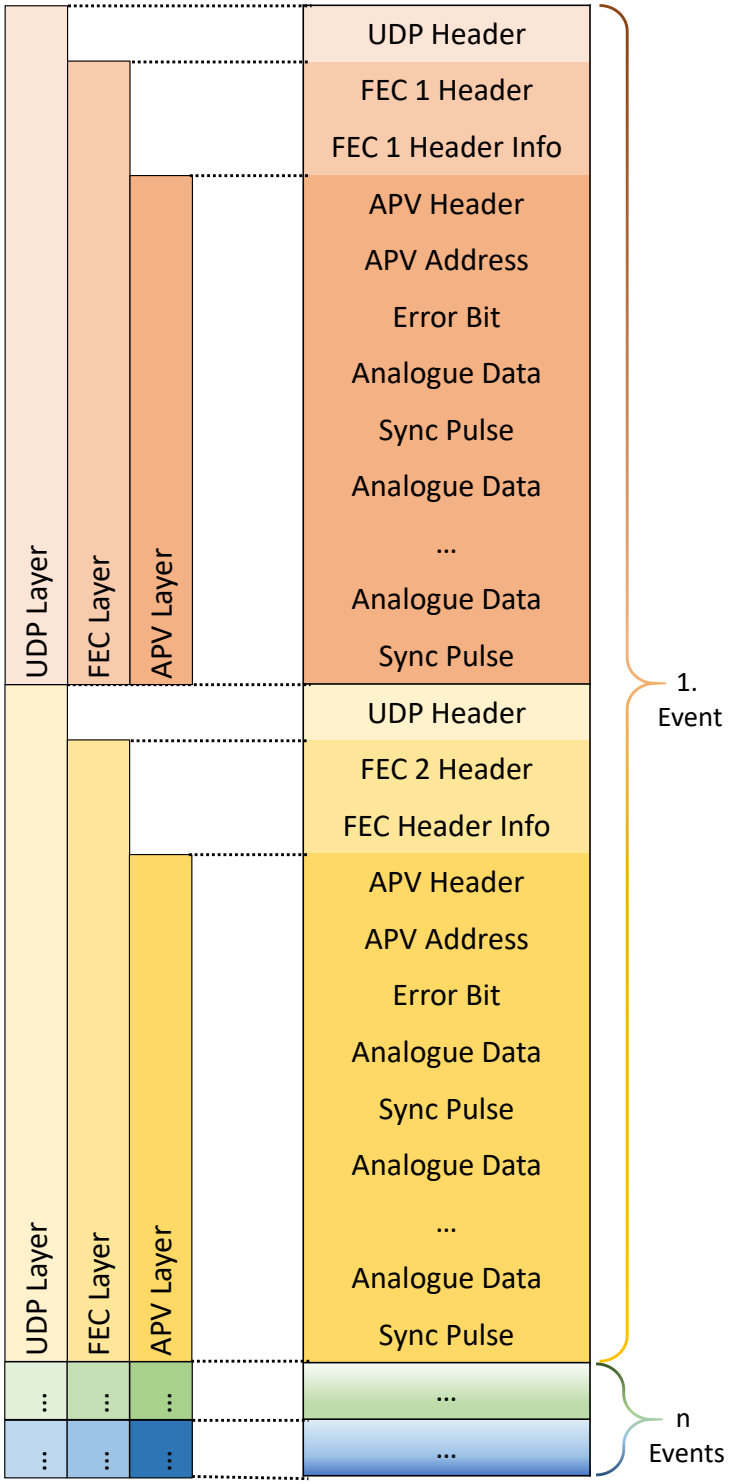

Figure 2.7: Schematic view of the structure of the SRS Data Format. The content of the different Layers (UDP, FEC and APV) is shown for a single event. [3] modified

2.3 Test Set up

GEM chamber and X-ray source are shielded in a copper box. The X-ray source is pointed to the x-z plane of the detector and mounted on the copper box. The X-ray beam covers the entire detector surface (see fig. 2.8) with a 120° X-ray cone. A gas bottle filled with Ar/CO_2 is connected to the GEM chamber via tubes to ensure a constant gas flow in the detector. The HV is applied to the GEM chamber by a HV power supply through a HV-filter. The SR-System is connected to the APVs and measurement PC as described above. Through the control software the relevant parameters like the X-ray source, the voltage between the drift cathode and readout plane and the recording of measurement data can be controlled at the same time. Pictures of the real set up can be found in A "Appendix".
For all measurements the X-ray source is run on a tube voltage of 40 kV and a tube current of 90 μA. An Ar/CO_2 gas flow of about 5 nl/h is set[2]. A set voltage can be entered manually at the control software. The actual applied voltage and the corresponding current, can be monitored. This output voltage and its corresponding current are the varied parameters specified in ch. 3.2.
In total three parameters are varied for the different measurements: The gain at the input stage of the multiplexers (preamplifier) at the APVs, the gain of the bias current at the multiplexers at the APVs and the HV/current applied to the chamber. The first of these is called MUXGAIN[3]. There are five selectable settings (1, 2, 4, 8, 16). In total a variation of ±10 % is possible[4]. The second is called IMUXIN. It can be adjusted in steps of 1 μA. The abbreviation for the applied current is I and the one for the voltage is HV. The concrete specification of values takes place in the chapter analysis together with the associated measured characteristic variables (see ch. 3.2).

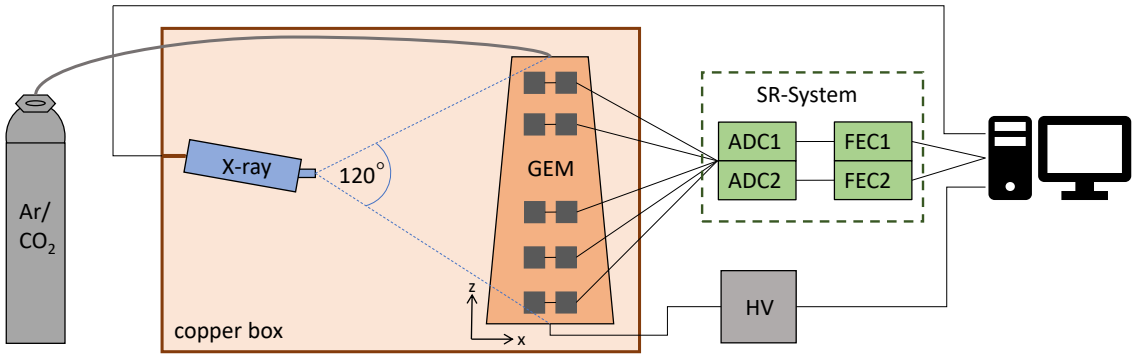

Figure 2.8: schematic view of the test set up, an Ar/CO_2 bottle and the HV are connected to the GEM chamber, the X-ray source targets the entire chamber, the APVs on the GEM chamber are connected to the SR-System (ADCs and FECs). The X-ray source, HV and the SRS can be controlled, read out and stored by the software on the measurement PC

[2]flow unit is norm litre per hour
[3]The unit of the MUXGAIN is unknown. In [1] 1 mA/mip. is given for an unknown detector.
[4]MUXGAIN variation from default (4): (-10, -5, 0, +5, +10) %

3 Analysis

First in this chapter the entire structure and some crucial points of the coded ”unpacker” are described in more detail. Second the analysis of the measured data by using the ”unpacker” is presented. Finally the results of the analysis are discussed with special emphasis on the temporal and spacial signal propagation.

3.1 ”Unpacker”-Code

In the following, the structure of the so-called ”unpacker” is described, especially in view of the peculiarities of the rawdata mode of the SR-System. A recorded datafile consists of information stored in the hexadecimal system, arranged in 2 16-bit words (i.e. 4-byte) packets. For the analysis of the different measurements it is essential to obtain the beginning of the analogue measured data and to automate this process. In the first step, the data file is read in, whereby the various header (*UDP, FEC and APV header*) and header information (*FEC and APV header info*) are stored separately from the analogue data. The *UDP* and the *FEC header* and *header information* have a fixed length, so they are easily to extract, in contrast to the *APV header* (see ch. 2.2.1). In the 4-byte long *FEC header info* detailed data information about the length of the *APV header* is stored in the first two bytes. According to formula `FEC_header_info[1]*256 + FEC_header_info[0]` the *APV header* length can be calculated. After the *APV header* and *header info* the analogue measured data begin. In a first step data are stored separately for FEC 1 and 2. Now the physical strips are mapped to the APV channels using the `APVch_to_strip()` function. The reverse mapping is possible using the function `strip_to_APVch()`. The used code is shown in fig. 3.1. In addition the output order of the APV numbers by the SR-System can be adapted to the physical order of the readout electronics on the chamber using the `get_sector()` function (see fig. 3.2). The measured data of an event are now structured in a vector of the same name with 3072 traces (total number of strips of the chamber) to which vectors with 21 data points (corresponds to the number of time bins) are assigned in each row. During the analysis it became apparent that there are events with a different length than standard, which therefore are called ”corrupted events”. Since this only affects about 1 % of recorded events, these events are stored separately and are no longer used for further analysis (see fig. 3.3). After these events are sorted out, the remaining ones are stored in a vector structure. It contains the analysable measurement data of all events of all strips with all time bins of the entire chamber.

In the next step the raw data is prepared for the analysis. An example for a signal in the inverted raw data is shown in fig. 3.4 by plotting the ADC count against 21 time bins of each of the 128 strips of a single APV. First, the baseline of the data is determined in order to invert the data and later differentiate signals from statistical fluctuations of these. For this purpose the median is taken from 21 time bins each at 1/3 of the absolute signal amplitude (see fig. 3.5). Note that the signal deflections drop in the raw data and thus the median is calculated in fig. 3.5 with 2/3, which corresponds to a median of 1/3 after inverting. First, the 21 time bins are sorted in increasing order of their values. The median is then the value that is 2/3 of the length of the array (note inversion). In this way a baseline of each strip is calculated. The median of 1/3 is used, since the included data also contain signals and the median is stable against outliers. These should not be considered for the calculation. The choice of this baseline determination is later also confirmed by the analysis (see ch. 3.2 length of the signal over time bins). Finally the data are being inverted.
A so called peak finder is used to find the signals in the measured data (see fig. 3.6). This is programmed in descending double-threshold order. Which means that in order to be

interpreted as a signal (”peak”), its first data point must reach a threshold above the previously determined baseline. The following data point in time bin must also reach a slightly lower second threshold. The two thresholds depend on the noise of the baseline and are calculated individually for each strip. The first threshold is seven times the standard deviation of a strip. The second threshold is set two standard deviations lower. This results in a minimum length of two time bins. Furthermore, at a later point in the code, not only the neighbouring time bins, but also the neighbouring strip and their time bins are evaluated with the second peak threshold. So that fake peaks can be separated from signals and then a temporal and a spacial analysis of the signals is possible. For further analyses, the highest global peak of each APV is also determined, since it is assumed that only one signal per event and APV is a real signal.
While analysing the data, it was noticed that channel 111 is to noisy to use the data of this strip. This means that even without an active X-ray source, i.e. mostly without external signal sources, a signal of constant hight is output for many events. One can see this signal by plotting ADC count against the time bins. In fig. 3.7 an example for APV 22 is shown. The points with about 1100 ADC counts all can be mapped to strip 111. Thus, this channel is eliminated in the whole analysis. There are some more noisy channels observable. By analysing the following noise measurement (ch. 3.2) a filter is defined to eliminate the most of the noise.

```
int Unpacker::APVch_to_strip(int APVch){
// mapping APV channel to physical srip
        int connector = (32 * ( APVch % 4 ) + 8 * (int)( APVch / 4 ) - 31
             * (int)( APVch / 16 ));
        if (connector % 2 == 0){
        return int(connector/2);
        }
        else{
        return int((connector-1)/2) + 64;
        }
}

int Unpacker::strip_to_APVch(int strip){
// mapping physical strip to position in timebin
        static int strip_to_APV_map[128] = {0, 16, 32, 48, 64, 80, 96,
           112, 4, 20, 36, 52, 68, 84, 100, 116, 8, 24, 40, 56, 72, 88,
           104, 120, 12, 28, 44, 60, 76, 92, 108, 124, 1, 17, 33, 49, 65,
            81, 97, 113, 5, 21, 37, 53, 69, 85, 101, 117, 9, 25, 41, 57,
           73, 89, 105, 121, 13, 29, 45, 61, 77, 93, 109, 125, 2, 18, 34,
            50, 66, 82, 98, 114, 6, 22, 38, 54, 70, 86, 102, 118, 10, 26,
            42, 58, 74, 90, 106, 122, 14, 30, 46, 62, 78, 94, 110, 126,
           3, 19, 35, 51, 67, 83, 99, 115, 7, 23, 39, 55, 71, 87, 103,
           119, 11, 27, 43, 59, 75, 91, 107, 123, 15, 31, 47, 63, 79, 95,
            111, 127 };

        if (( strip >= 0 )&&(strip <= 127)){
                return ( strip_to_APV_map[strip]);
        } else {
        std::cout<< "ERROR: Strip out of range!" << std::endl;
        return -1;
        }
}
```

Figure 3.1: Code for mapping APV channel to strip

```
int Unpacker::getSector(int fec, int apv){
//map apv to physical sectors
        static int apv_new[24] =
           {24,19,22,23,10,11,16,17,18,13,21,20,12,7,6,1,9,8,4,5,3,2,15,14};

return (apv_new[fec*12+apv]);
}

int Unpacker::getSector_onlyAPV(int apv){
//map apv to physical sectors
        static int apv_new[24] =
           {24,19,22,23,10,11,16,17,18,13,21,20,12,7,6,1,9,8,4,5,3,2,15,14};

return (apv_new[apv]);
```

Figure 3.2: Code for mapping APV to sector

```
//collect events with corrupted data
if (!(data_FEC1[apv].size()==4000)){
        isCorruptedEvent = true;
        std::vector<int> info1;
        info1.push_back(event_cnt-1);
        info1.push_back(1);
        info1.push_back(apv);
        CorruptedData.push_back(info1);
        info1.clear();
}
if (!(data_FEC2[apv].size()==4000)){
        isCorruptedEvent = true;
        std::vector<int> info2;
        info2.push_back(event_cnt-1);
        info2.push_back(2);
        info2.push_back(apv);
        CorruptedData.push_back(info2);
        info2.clear();
}
```

Figure 3.3: Code snipped for separating corrupted events from events without complications

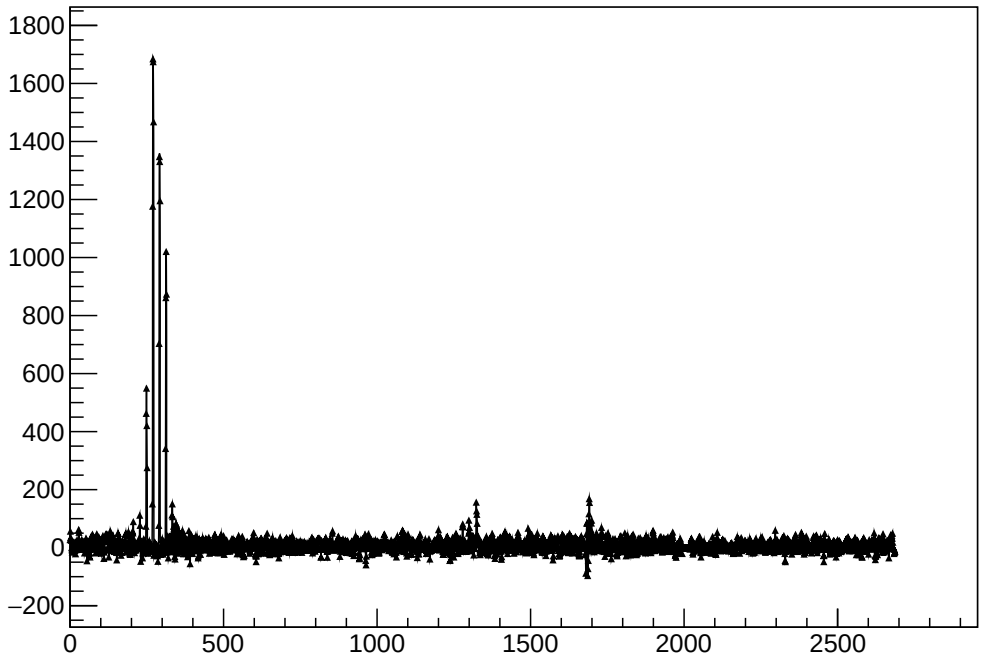

Figure 3.4: 21 time bins for each of the 128 strips of a single APV for a single event. Plot is made after baseline inverting. The four main peaks show the same signal but in three neighbouring strips.

```
//calculate baseline for each strip
int len = 0;
for (unsigned int evt = 0 ; evt < data.size() ; evt++){
        for (int fec = 0 ; fec < 2 ; fec++){
                for (int apv = 0 ; apv < 12 ; apv++){
                        for (int strip = 0; strip <128; strip++){
                        len = 0;
                        median_data.clear();
                        for (int i = 0; i <21; i++){
                                if (strip == 111 ){
                                        median_data.push_back(data[evt][
                                            fec*1536 + apv*128 + strip -1][
                                            i]);
                                }else{
                                        median_data.push_back(data[evt][
                                            fec*1536 + apv*128 + strip][i
                                            ]);
                                }
                        }
                        std::sort (median_data.begin(), median_data.end()
                            );
                        len = median_data.size(); //len = 21
                        data_baseline[evt][fec*1536 + apv*128 + strip][0]
                             = median_data[(2*len)/3];
                        }
                }
        }
}
```

Figure 3.5: Code snipped for baseline calculation by 1/3 median

```
void Unpacker::PeakFinder(){
        int peak_cutoff = 0; //first threshold
        int peak_cutoff_2 = 0;  //second sthreshold
        int event = 0;
        int fec = 0;
        int apv = 0;
        int strip = 0;
        int timebin = 0;
        int peak_length = 0;
                for (unsigned int i = 0; i < data_inverted.size(); i++){
                event = i/64512;
                fec = (i - event*64512)/32256;
                apv = (i - event*64512 - fec*32256)/2688;
                strip = (i - event*64512 - fec*32256 - apv*2688)/21;
                //calculate thresholds by using the baselinenoise
                peak_cutoff = round(7*mean_bar[(apv + fec*12)*128+strip])
                    ;
                peak_cutoff_2 = round (5*mean_bar[(apv + fec*12)*128+
                    strip]);
                if (data_inverted[i] > peak_cutoff){
                        std::vector<int> hInfo;
                        std::vector<uint32_t> hdata;
                        timebin = (i - event*64512 - fec*32256 - apv*2688
                            -strip*21);
                        hInfo.push_back(event);
                        hInfo.push_back(fec);
                        hInfo.push_back(apv);
                        hInfo.push_back(strip);
                        hInfo.push_back(timebin);
                        peak_length = -1;
                        for (int j = 0; j < (21-timebin); j++){  //legth
                            of 21 time bins
                                if (data_inverted[i+j] > peak_cutoff_2){
                                        hdata.push_back(data_inverted[i+j
                                            ]);
                                        peak_length = j;
                                }else{
                                        break;
                                }
                        }
                        if ( peak_length <= 1) hInfo.clear();
                        if ( hInfo.size() > 0) peak_data[hInfo] = hdata;
                        hInfo.clear();
                        hdata.clear();
                }
                i=i+peak_length;
        }
}
```

Figure 3.6: Code for the double-threshold peak finder

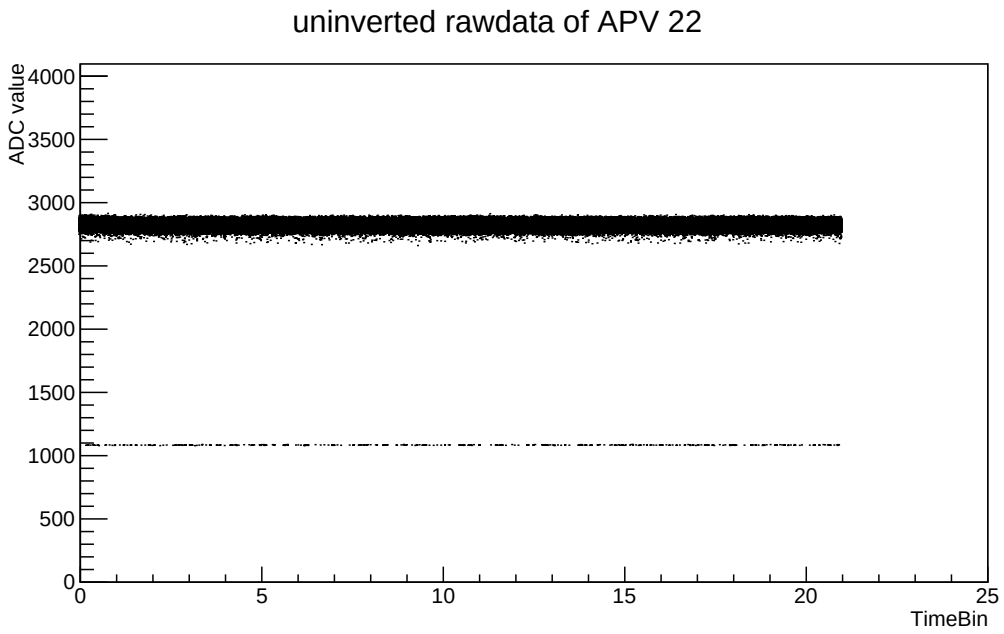

Figure 3.7: Raw data (not inverted) overlayed for many events of APV 22, ADC value means ADC count. One can see a line at about 1100 ADC counts. By closer examination of the data around 1100 ADC counts it is found out, that only strip 111 causes this data points. After being identified as a noisy strip it is eliminated.

3.2 Data Analysis

The two characteristic indicators of spacial and temporal propagation of signals are considered. Firsts the number of neighbouring strips over which a signal is distributed (`#strips`) is looked at and second the time spread (`#timebins`), i.e. over how many time bins the measured signal is distributed. By varying different parameters it is tried to optimise the measurement of signals. Besides the parameters set on the detector and SR-System (see ch. 2), the selection of the peak finder thresholds (see ch. 3.1) plays an important role. All following values are given in decimal notation.

3.2.1 Noise Measurement

At first the influence of different high voltages and MUXGAIN settings on the noise and the position of the baseline is measured. All noise measurements are taken without X-ray source and contain about 1.000 events each. The IMUXIN is set to the default value (16). It is investigated, whether the intensity of the noise level changes while varying the voltage at constant MUXGAIN, and than while changing the MUXGAIN at constant voltage. The MUXGAIN can be changed between 1 and 16 in steps given by the system (see tab. 3.1). For this purpose, the mean value and standard deviation of the ADC count of the 128 strips of each APV are determined. By this, as in ch. 3.1, an estimate for the two peak thresholds is obtained, which is recalculated for all subsequent measurements. The fluctuation of the baseline of the individual strips can also be seen in the following plots. In fig. 3.8, fig. 3.9 and fig. 3.10 the ADC count is plotted against the strip-number. As an example, only three plots are shown here, first with the whole baseline for MUXGAIN 1 and 608 μA, second with the maximum current difference and MUXGAIN 1 and third with MUXGAIN of 1, 4 and 16 and 627 μA. The values for the first and second threshold obtained of these plots, are exemplary displayed in tab. 3.2. To make it clearer the mean value of each APV is shown (and not the threshold of each strip). Moreover the position of the baseline without a zero shift is observed. In fig. 3.11 the ADC count is plotted against the strips. The position of the baseline for MUXGAIN 1 and 16 is shown exemplary for one voltage. As the behaviour between the MUXGAIN steps is linear, these plots are representative for the whole measurement series.

MUXGAIN	I /μA	HV /V	IMUXIN /μA
1	608	3200	16
	627	3300	
	646	3400	
2	608	3200	16
	627	3300	
	646	3400	
4	608	3200	16
	627	3300	
	646	3400	
8	608	3200	16
	627	3300	
	646	3400	
16	608	3200	16
	627	3300	
	646	3400	

Table 3.1: Settings of the noise measurements; IMUXIN on default, no X-ray source

In fig. 3.8 the ADC count of the zero shifted baseline mean is different for each strip. The means are equally distributed around zero. To study the distribution of the strip means in more detail, only an extract of 256 strips (two APVs) in fig. 3.10 and 128 strips (one APV) in fig. 3.9 are shown. In all of these plots one can see blocks of 16 strips each with similar position and height of the error bars. These blocks are caused by the multiplexer, which treats the strips as packages of 16 strips. For each package the baseline drifts to higher ADC counts. Moreover one can see a pattern of rising and descending packages, which repeats itself for every 128 strips, so for each APV. This shift has no impact on the peak finder, because the baseline is corrected for each strip individually.
In fig. 3.10 the shift of the baseline while varying the MUXGAIN can be observed. For higher MUXGAIN the strip means are drifting more apart than for lower. An increase of the standard deviation for higher MUXGAIN can be observed. Moreover in fig. 3.9 there is no baseline shift while varying the current from 608 μA over 627 μA up to 646 μA.
The thresholds for the peak finder are calculated from the standard deviation as described in ch. 3.1. One can see that even at low MUXGAIN there are high fluctuations from 1 to 157 ADC counts (see tab. 3.2) between the thresholds of each APV. With increasing gain the standard deviation of the baseline mean value also increases[5]. A dynamic threshold is therefore justified.
In fig. 3.11 the shifting of the baseline caused by change of the MUXGAIN is shown. The average ADC count of the strips decreases during the increase by the MUXGAIN. For MUXGAIN 1 the baseline is located at about 2800 ADC counts, for MUXGAIN 16 at about 2400 ADC counts. The difference of the ADC count between the APVs is just slightly changing. Different currents have no effect on the position of the baseline.

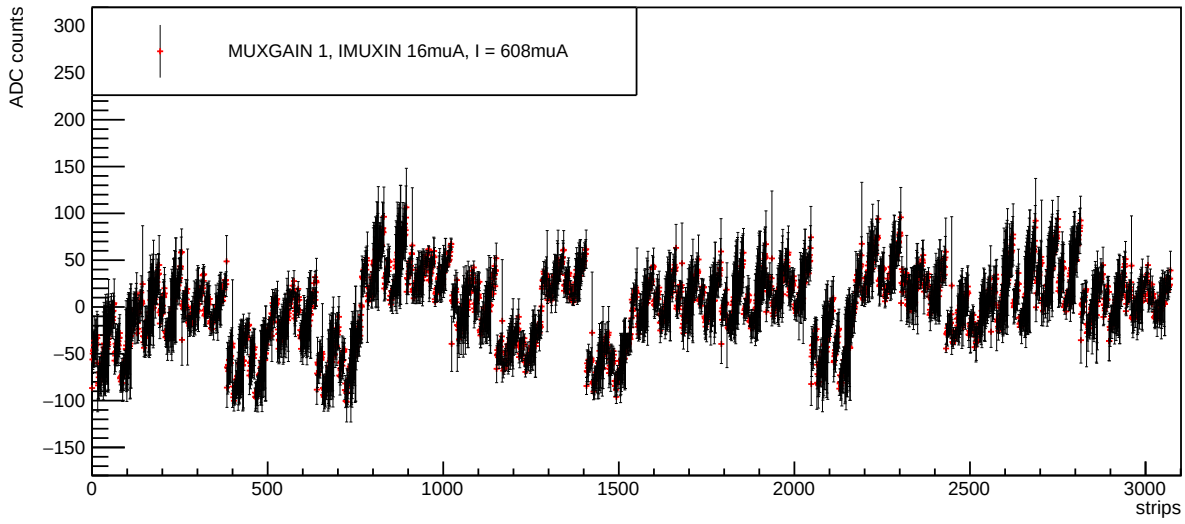

Figure 3.8: Mean of the ADC count for each strip and the corresponding standard deviation of baseline noise. The overall strip ADC count average is shifted to zero. 3072 strips (all APVs) are shown. X-ray source turned off. The means are equally distributed around zero. There is a shift of the means due to the variation of the MUXGAIN.

[5]Since the peak thresholds are automatically calculated for each measurement and only the values for MUXGAIN 1 are shown as an example, this is not shown here.

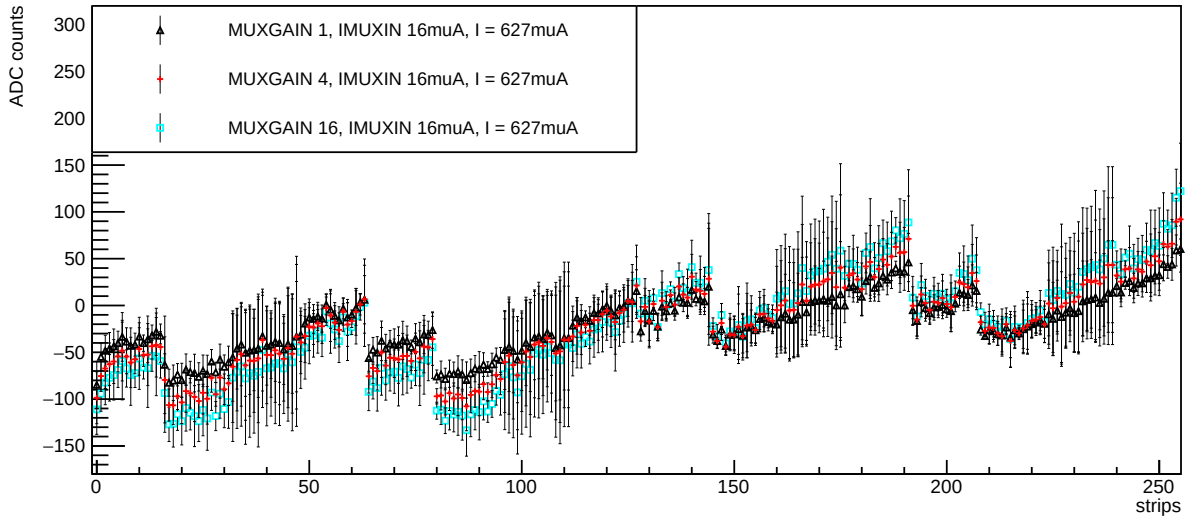

Figure 3.9: Mean of the ADC count for each strip and the corresponding standard deviation of baseline noise. The overall strip ADC count average is shifted to zero. 256 strips (two APVs) are shown. X-ray source turned off. The means are equally distributed around zero. There is no shift of the means due to the variation of the current.

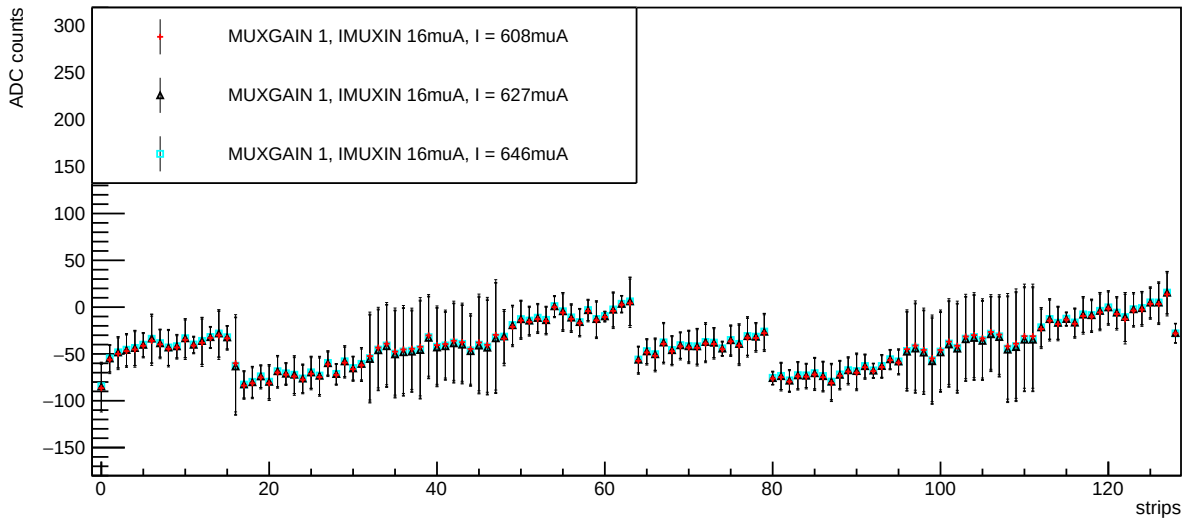

Figure 3.10: Mean of the ADC count for each strip and the corresponding standard deviation of baseline noise. The overall strip ADC count average is shifted to zero. 128 strips (one APVs) are shown. X-ray source turned off.

APV	threshold 1	threshold 2
1	222	150
2	168	100
3	103	61
4	222	156
5	138	86
6	224	157
7	136	64
8	62	22
9	137	80
10	144	103
11	70	30
12	180	131
13	124	71
14	122	69
15	161	93
16	113	59
17	229	154
18	100	43
19	94	47
20	139	88
21	180	100
22	140	69
23	136	80
24	90	50

Table 3.2: Peak thresholds in ADC counts (seven (1) and five (2) standard deviations from the baseline) of all APVs calculated by mean of the strip baselines outlined by the peak finder exemplary. For MUXGAIN 1 at 608μA and 3200 V with IMUXIN on default and X-ray source turned off.

To examine, if the thresholds suppresses the baseline noise reliable, some control plots are generated. The number of peaks found by the peak finder is plotted against the position of the peak in the 128 strips, the 21 time bins and the 24 APVs (see fig. 3.12). The data of all APVs and all events are overlayed. The plots show the results for MUXGAINs from 1 to 16. As the X-ray source is absent, no peaks expected to be seen in any of these plots. Furthermore the number of peaks is plotted to the integral over the peaks in ADC count with a logarithmic y-axis (see fig. 3.13).
It is obvious, that the peak thresholds can not suppress all the baseline noise. In the upper plot of fig. 3.12 one can see some single very noisy strips and some with only a low noise number. In the middle plot there can not be identified any suspicious time bins. The lower plot shows some single very noisy APVs (e.g. APV 8), some slightly noisy APVs and only a few APVs without any peaks. Moreover one can see, that the noise level rises with increasing MUXGAIN. In fig. 3.13 one can see a high peak at very low ADC counts (until 400 ADC counts) with a tail up to 6000 ADC counts.

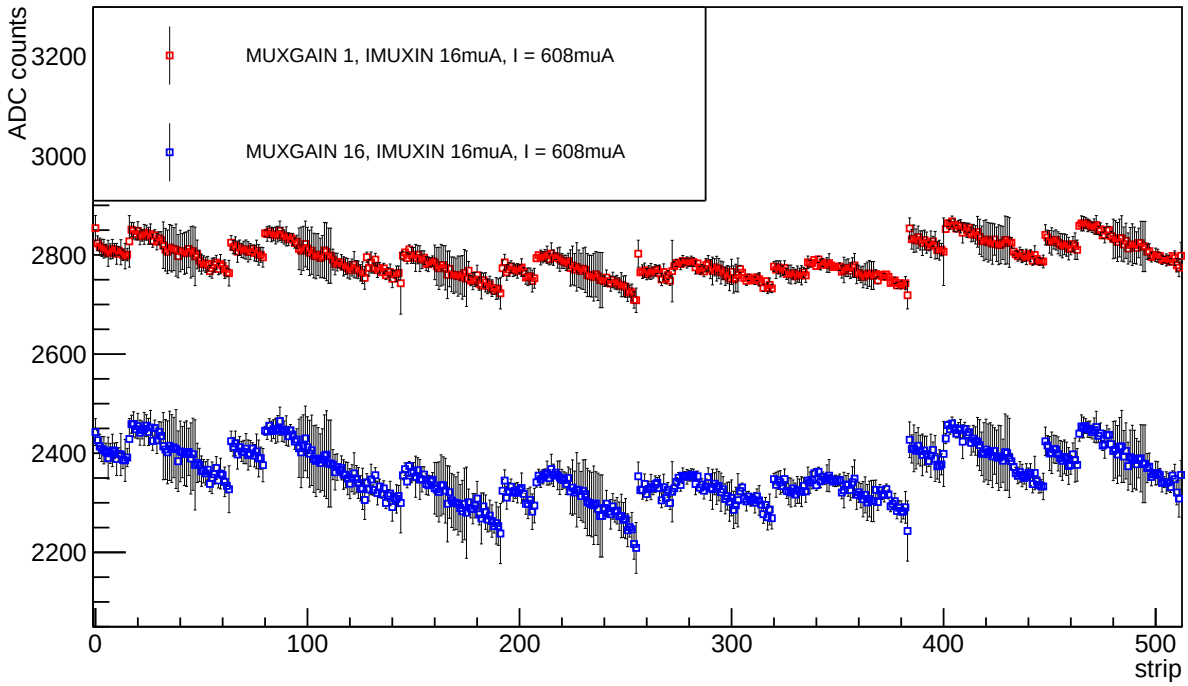

Figure 3.11: Mean of the ADC count for each strip and the corresponding standard deviation of baseline noise. The position of the baselines in the ADC count measured with different MUXGAINs. 512 strips (four APVs) are shown. X-ray source turned off. The baseline has different positions due to the different MUXGAINs.

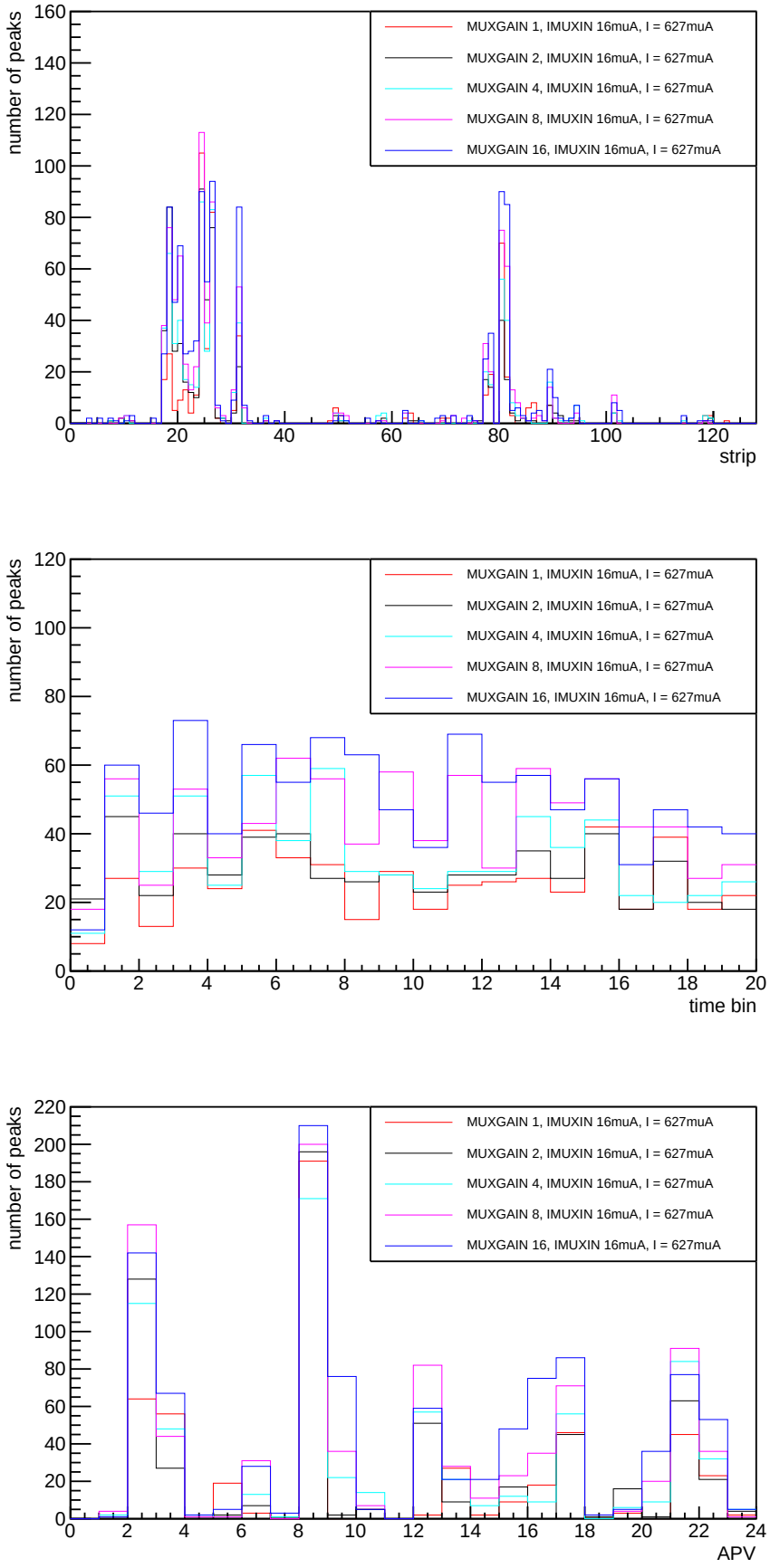

Figure 3.12: Control plots; upper for the number of measured peaks plotted against the strips, middle for the number of measured signals plotted against the time bins, lower for the number of measured peaks plotted against the APV number. X-ray source turned off. There are many detected peaks, although there is no X-ray source. So this peaks must be noise.

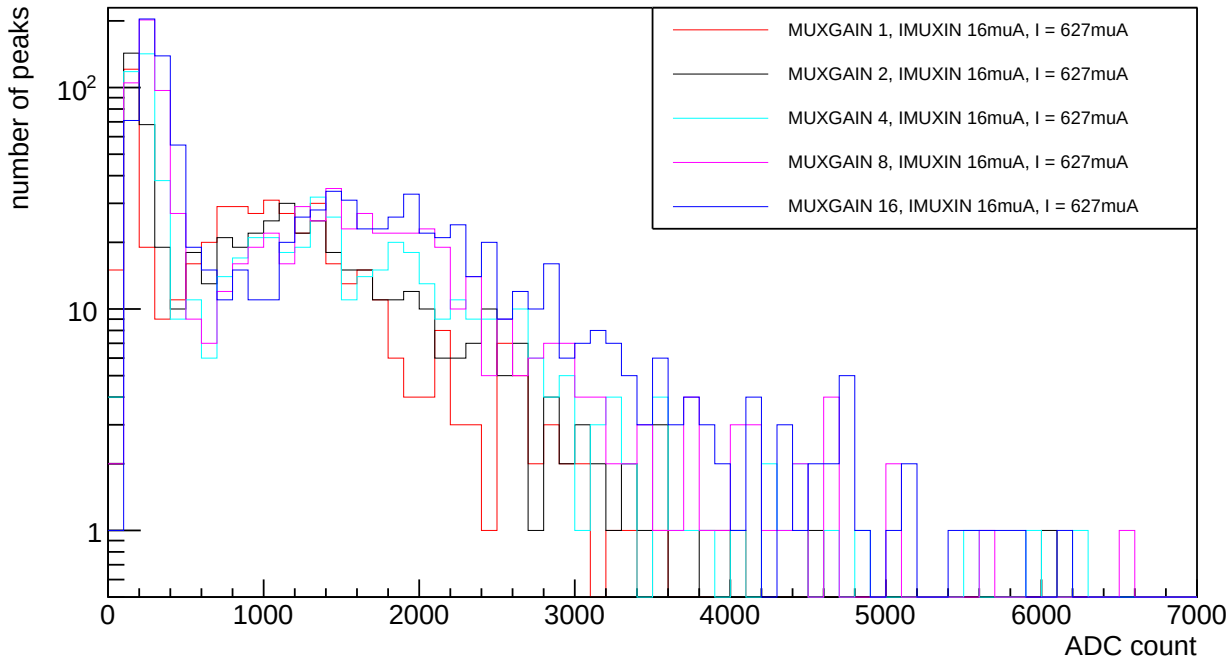

Figure 3.13: Comparison of the Integral ADC count of the peaks measured with different MUXGAINs. The y-axis is plotted logarithmic.There are many detected peaks, although there is no X-ray source. So this peaks must be noise.

The high peak in fig. 3.13 is mainly noise and should be suppressed, so a new selection criterion for signals is added. If the peak has an integral lower than 400 ADC counts[6] it is cut. In the following this cut is called "stage 1". To study which APVs, strips and time bin combinations are the most noisy one the APV number is plotted against the strip and the time bin, while the number of peaks is colour coded. (see fig. 3.14, 3.15, 3.16, 3.17, 3.18 and 3.19). The most noisy ones are disabled. This selection of single APV-strip combinations together with stage 1 is called "stage 2" in the following.
In fig. 3.14 and 3.17 one can see the noisy APVs, strips and time bins. In fig. 3.15 and 3.18 the noise level after cut-off stage 1 is shown. Some noisy strips disappear completely (e.g. 51) and most of the strips have a strongly reduced noise level (e.g. strip 24, 80). The APVs 2 and 8 have still an outstanding noise level. For stage 2 the noisiest three APV-strip combinations are selected: APV 2 & strip 20, APV 8 & strip 24 and APV 8 & strip 26. In fig. 3.16 and 3.19 one can see the decrease of the noise level again. In comparison to stage 1 the maximal number of peaks is halved.
By checking the control plots (see fig. 3.20) and the ADC count integral (see fig. 3.21) again for the different stages one can see a clear improvement of the noise filter. This is important for the next measurement, where real signals have to be distinguished from peaks caused by noise.

[6]This value is set global for all measurements.

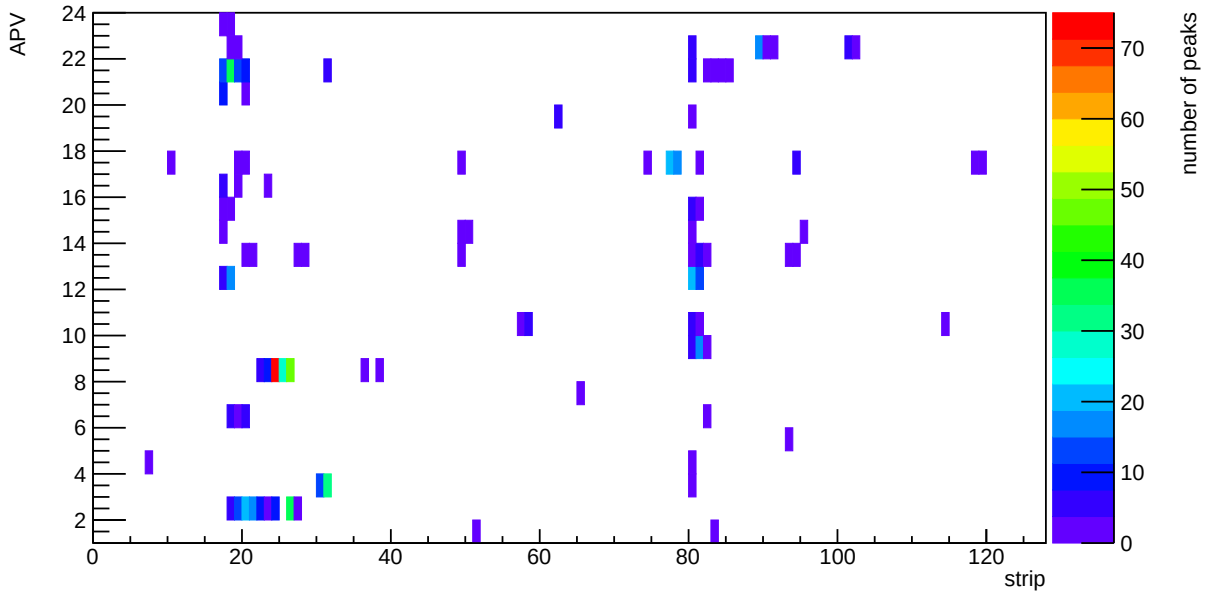

Figure 3.14: Number of peaks (colour coded) found in the noise measurement resolved by APV and strip number without any filter. Measured with MUXGAIN 4 and a current of 627 μA. X-ray source turned off.

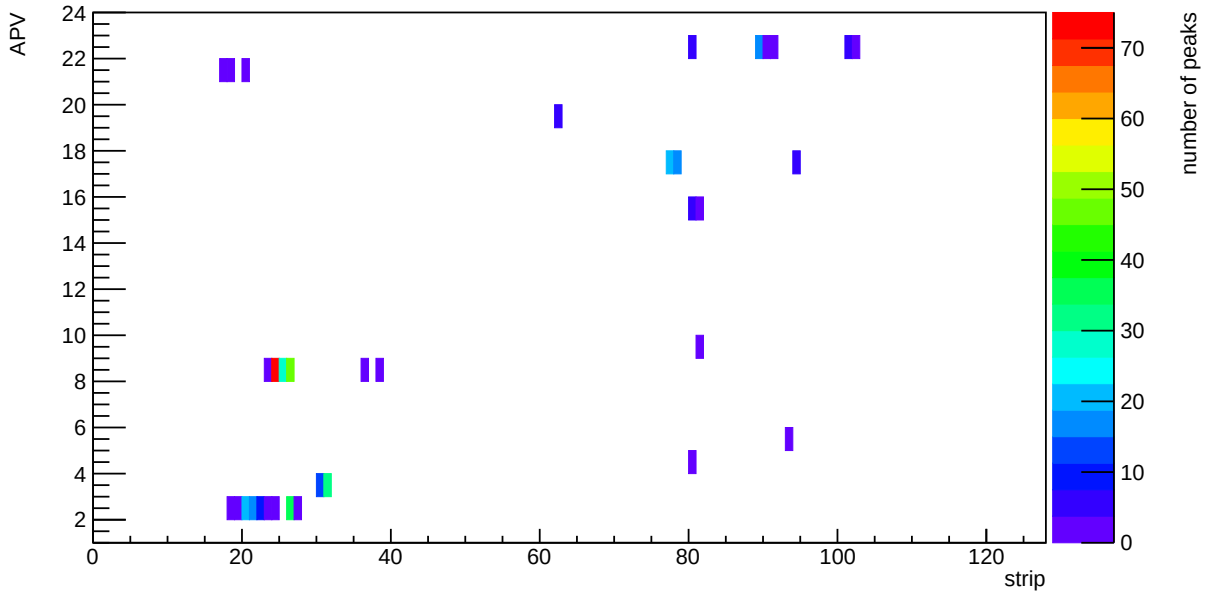

Figure 3.15: Number of peaks (colour coded) found in the noise measurement resolved by APV and strip number filtered with stage 1. Measured with MUXGAIN 4 and a current of 627 μA. X-ray source turned off.

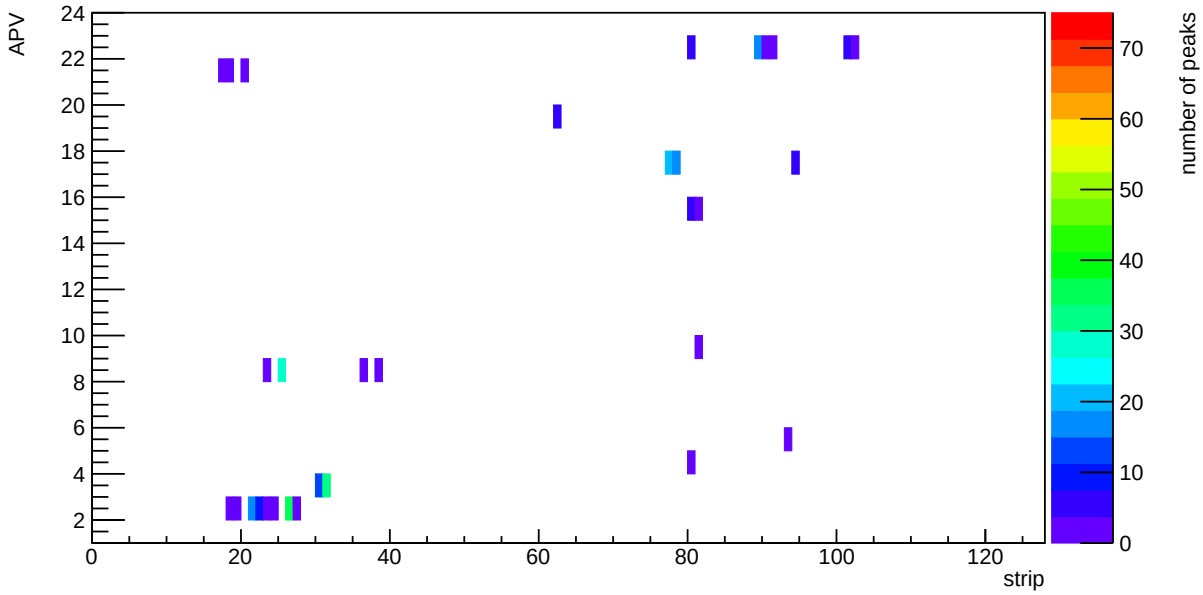

Figure 3.16: Number of peaks (colour coded) found in the noise measurement resolved by APV and strip number filtered with stage 2. Measured with MUXGAIN 4 and a current of 627 μA. X-ray source turned off.

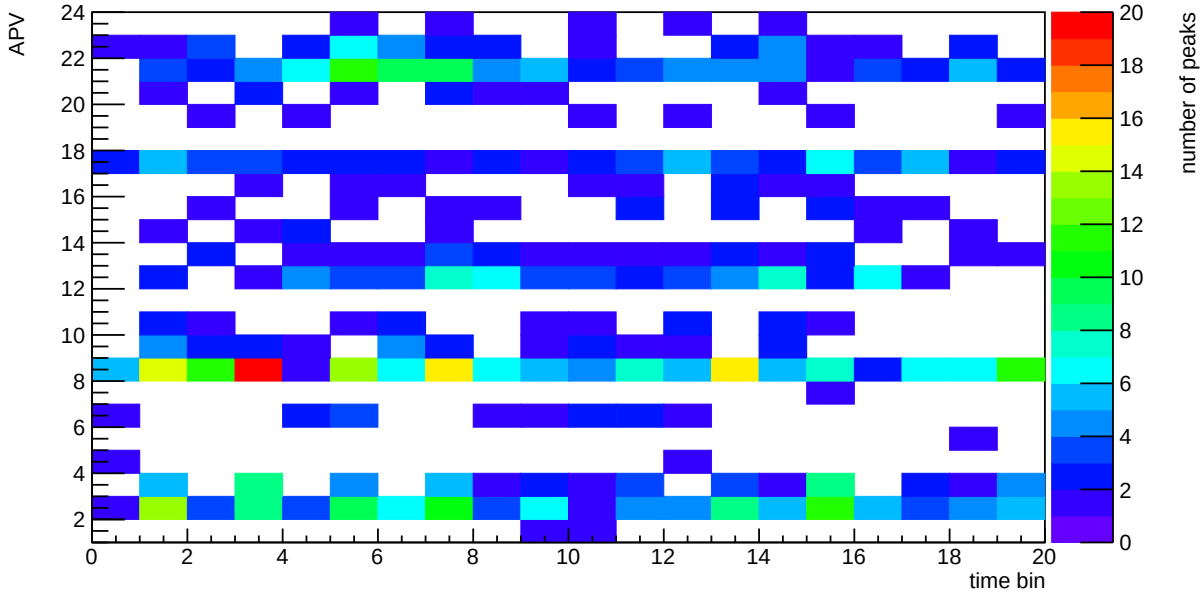

Figure 3.17: Number of peaks (colour coded) found in the noise measurement resolved by APV and time bin number without any filter. Measured with MUXGAIN 4 and a current of 627 μA. X-ray source turned off.

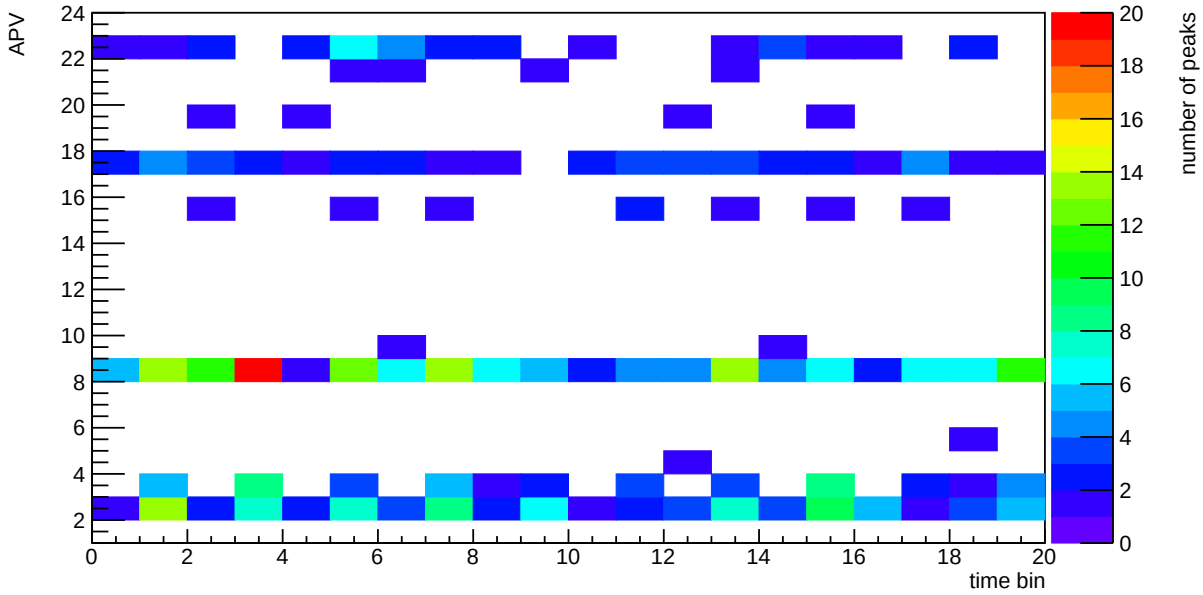

Figure 3.18: Number of peaks (colour coded) found in the noise measurement resolved by APV and time bin number filtered with stage 1. Measured with MUXGAIN 4 and a current of 627 μA. X-ray source turned off.

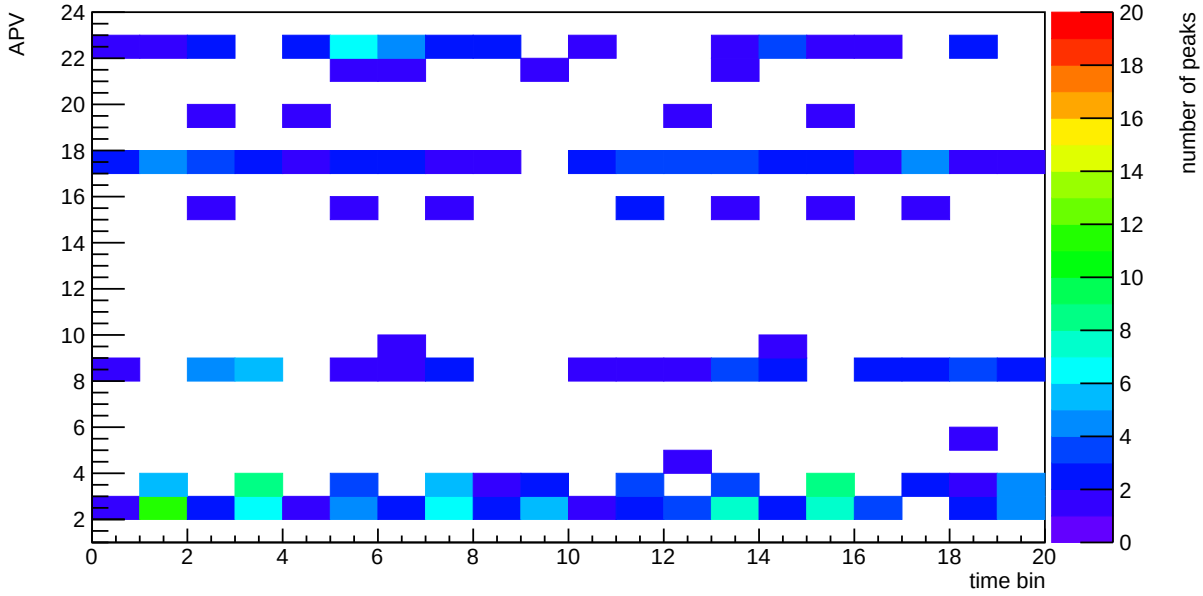

Figure 3.19: Number of peaks (colour coded) found in the noise measurement resolved by APV and time bin number filtered with stage 2. Measured with MUXGAIN 4 and a current of 627 μA. X-ray source turned off.

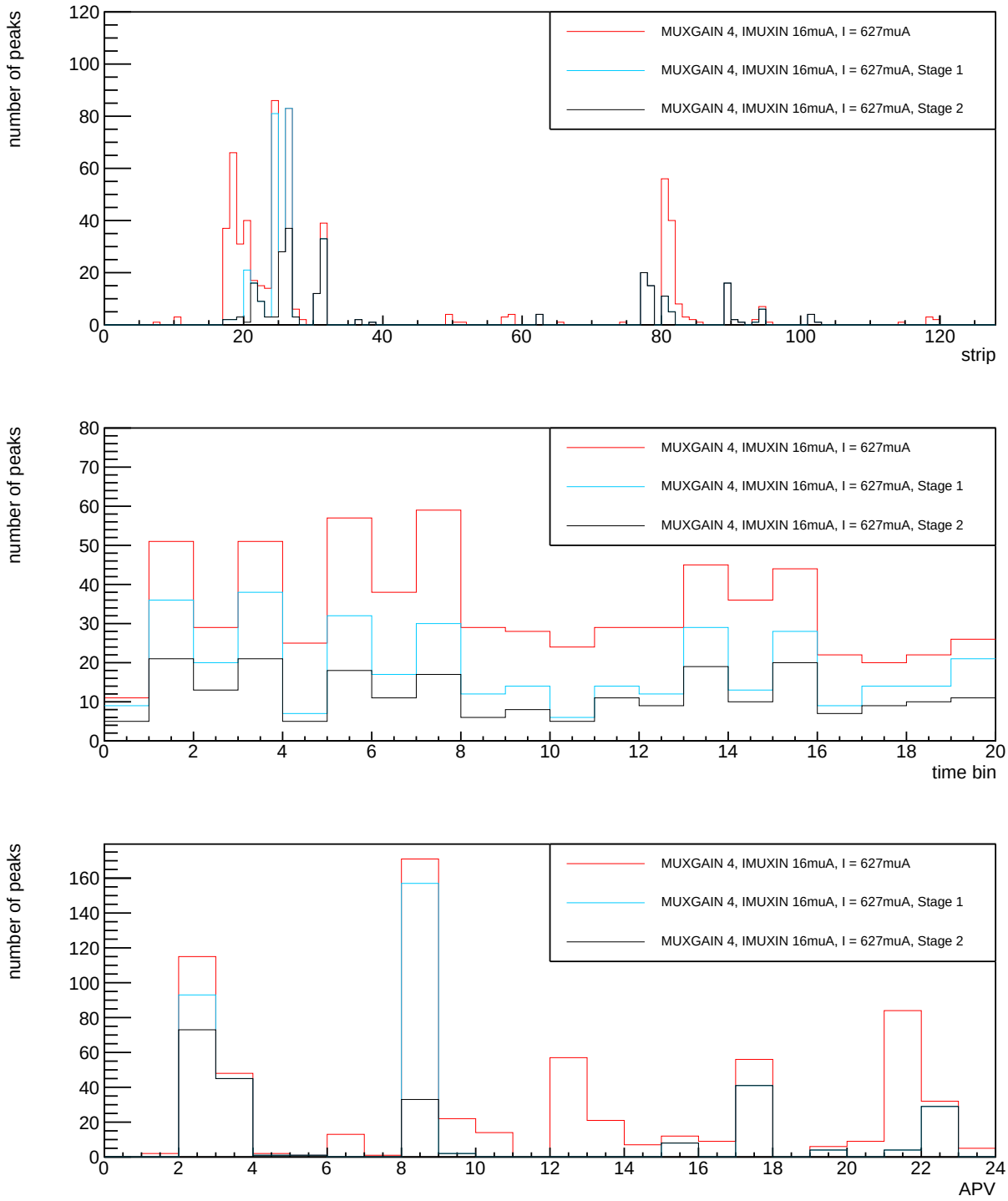

Figure 3.20: Comparison of the control plots with and without filter stages; upper for the number of measured peaks plotted against the strips, middle for the number of measured signals plotted against the time bins, lower for the number of measured peaks plotted against the APV. X-ray source turned off. One can see a reduction of the noise due to the filter steps.

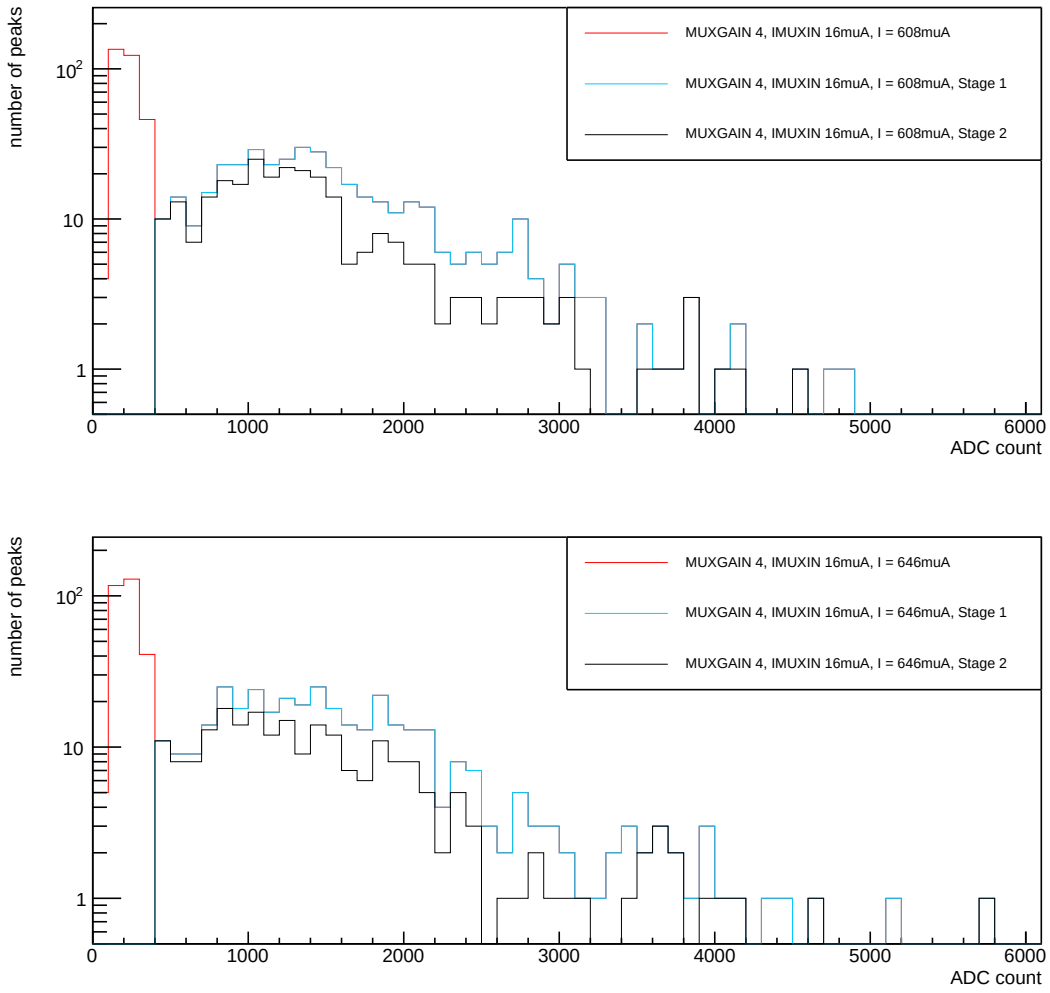

Figure 3.21: Comparison of the Integral ADC count of the peaks with and without filter stages. The y-axis is plotted logarithmic. One can see a reduction of the noise due to the filter steps.

3.2.2 Variation of MUXGAIN and I/HV with X-rays

The characteristic indicators `#strips` and `#timebins` of the signals are analysed when changing the MUXGAIN. Measurements are now taken with active X-ray source, about 10.000 events each and IMUXIN on default (16). For this purpose, the MUXGAIN is varied between 1 and 16 as in the noise measurement before. In addition, the behaviour when the applied current changes from 608 μA to 646 μA is also considered (see tab. 3.3).

MUXGAIN	I /μA	HV /V	IMUXIN /μA
1	608	3200	16
	627	3300	
	646	3400	
2	608	3200	16
	627	3300	
	646	3400	
4	608	3200	16
	627	3300	
	646	3400	
8	608	3200	16
	627	3300	
	646	3400	
16	608	3200	16
	627	3300	
	646	3400	

Table 3.3: Settings of the measurements while variation of the MUXGAIN and the I/HV; I in μA, HV in V, IMUXIN on default, Active X-ray source.

First, three control plots are created to see temporal and spacial distribution of the signals. Thus, e.g. an overload of the detector at too high gain or voltage or other inconsistencies can be easily observed or excluded. The number of signals found by the peak finder is plotted against their position in the 128 strips, the 21 time bins and the APV number (see fig. 3.22). The data of all APVs and all events are overlayed. If there are no corruptions in the measurement, an approximate equal distribution of the signals over strips and time bins is expected for all three plots, respectively. Furthermore the number of peaks is plotted to the integral over the peaks in ADC count (see fig. 3.23). Here only the plots for a current of 627 μA are shown. The other plots can be found in "appendix" A.

The expectations for the plots in fig. 3.22 are largely fulfilled in all cases. One can see a rise of absolute number of detected signals in relation to higher MUXGAIN in all plots. In the upper one there are about 10 strips which detected more signals than the average of the other strips. These suspicious strips are the same as in the noise measurement. So the higher number of peaks for this strips is caused by noise which were not filtered by stage 1 and 2. Moreover one can see again the pattern of blocks of 16 strips caused by the multiplexer, as in the baseline plots of the noise measurement (see ch. 3.2.1).
The middle plot gives a slightly different picture. The distribution of the peaks over the time bins is equal except for the first two time bins. This can be explained with the emergence of this plot: The position of maximum (in ADC counts) of every peak in the 21 time bins is filled in the histogram. If there is a high signal some time bins before the record of the data starts, the tail of this signal could be measurable in the first time bins of the next event. This

tail increases with higher MUXGAIN. So in the first time bins are more peaks counted than in the other.
The lowest plot shows a nearly equal distribution of the peaks over the APVs. A slight increase to higher numbers of APVs can be noticed. This can be explained by the design of the GEM chamber. The surface size increases for sectors (according to APV number) at the wider side of the detector (see ch. 2) and with a larger surface more signals can be detected. These three plots are nearly the same for all recorded currents and HV. Only the absolute number of detected signals is changing.
In the plot in fig. 3.23 the add up ADC count of all strips and time bins of each peak is shown. So it is an indicator for the temporal and spacial enhancement of the signals. One can see two peaks. The main peak is found around 1500 ADC counts. The second peak is about 50 peak counts lower for all MUXGAINs. Its position on the x-axis shifts for higher MUXGAIN from 4500 ADC counts to 7500 ADC counts. This can also be observed for increasing current. These plots can be found in "appendix" A. For MUXGAIN 16 there is a very high peak right after the cut-off at 400 ADC counts of stage 1. Probably this is amplified noise not suppressed by stage 1 and 2. The tail of the distribution becomes longer for higher MUXGAIN and HV. The origin of this is further investigated in the next paragraph.

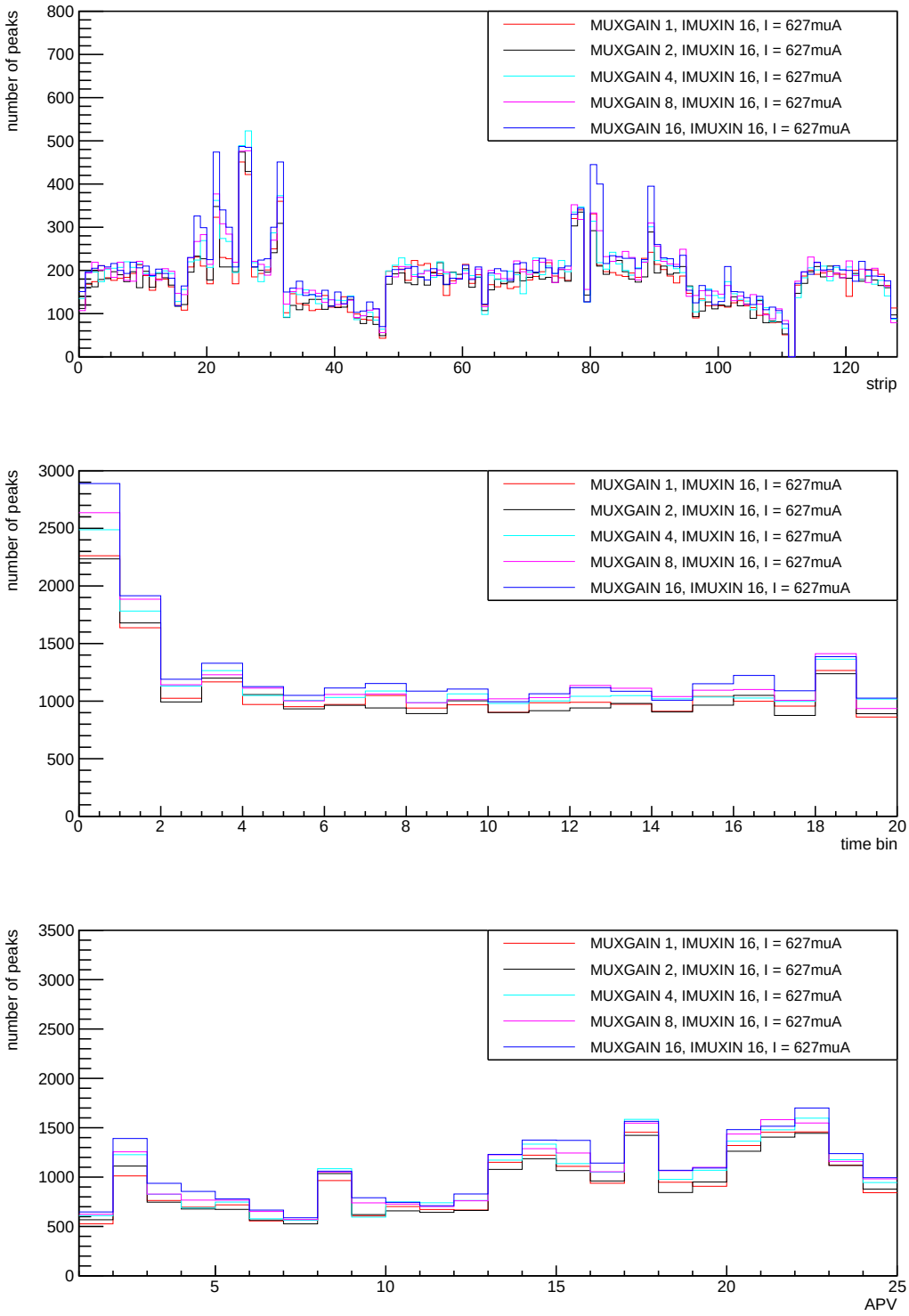

Figure 3.22: Control plots filtered with stage 2; upper for the number of measured peaks plotted against the strips, middle for the number of measured signals plotted against the time bins, lower for the number of measured peaks plotted against the APV number. Active X-ray source.

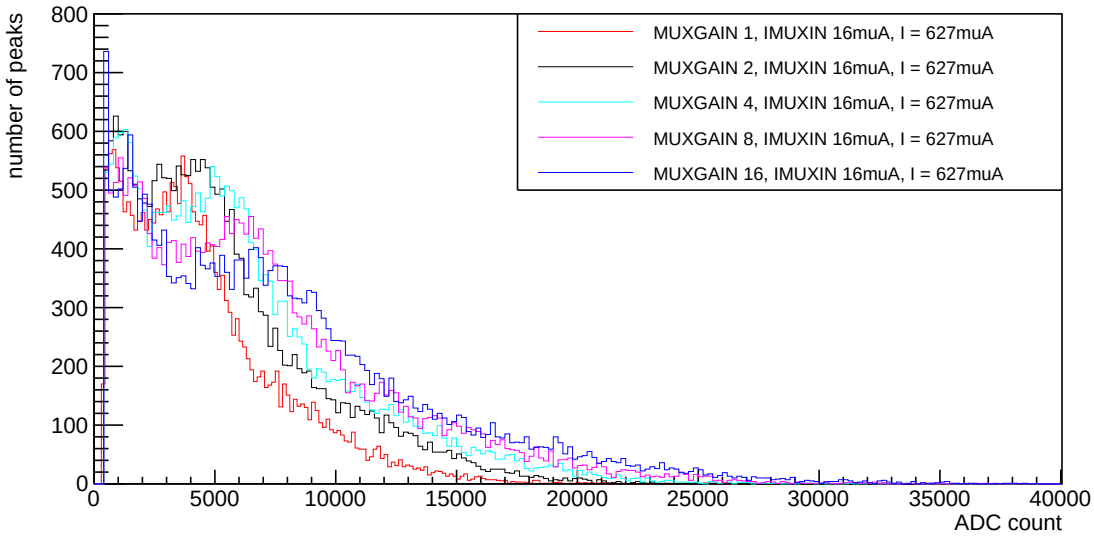

Figure 3.23: Integral over the ADC count of the signals with filter stages for different MUXGAINs. Active X-ray source.

Next the `#strips` and `#timebins` are considered. The signals identified with the peak finder are arranged to their width in time and space by using the standard deviation of their distribution. The RMS of the number of hit neighbouring strips and time bins is plotted against the normed number of time bins. In fig. 3.24 the results for all MUXGAINs from 1 to 16 and a current of 627 μA are shown as examples. The remaining plots for currents of 608 μA and 646 μA can be found in "appendix" A.
The upper plot of fig. 3.24 shows a main peak for 0.5 strips which is set to the left for all measured MUXGAIN and currents. For higher MUXGAIN the intensity of the main peak goes down caused by an increasing number of hits in higher strips. The tail of the distribution shows a maximal spacial width of 1.75 strips. It does not change significantly for different IMUXIN or currents. The distribution in the lower plot is different to the upper one. The main peak is placed at 1.5 time bins for a current of 608 μA and at 2.25 time bins for 627 μA. So there is a shift to higher number of serial time bins due to increasing current. There is no tail as in the upper plot. The maximal number of neighbouring time bins is close to the main peak. The number of peaks in higher time bins increases for increasing MUXGAIN. For the current step from 627 μA to 646 μA the number of peaks in higher time bins increases, too. The step from 608 μA to 627 μA shows no significant change. For both plots one can see outliers in the length of the signals. It can not be differentiated if these are noise, transients or real signals. In tab. 3.4 the position of the main peak and the maximal width in strips and time bins is shown.

MUXGAIN	I	std. dev. of `#strips`		std. dev. of `#timebins`	
		max. number	max. width	max. number	max. width
1-16	608	0.5	1.75	2.0	3.5
	627	0.5	1.75	2.25	3.5
	646	0.5	2.0	2.5	3.75

Table 3.4: Spacial (`#strips`) and temporal (`#timebins`) dimension of the signals by analysis with their standard deviation (std. dev.); I in μA, max. number refers the position of the mean peak in strips or time bins, max. width marks the maximal standard deviation value in strips or time bins

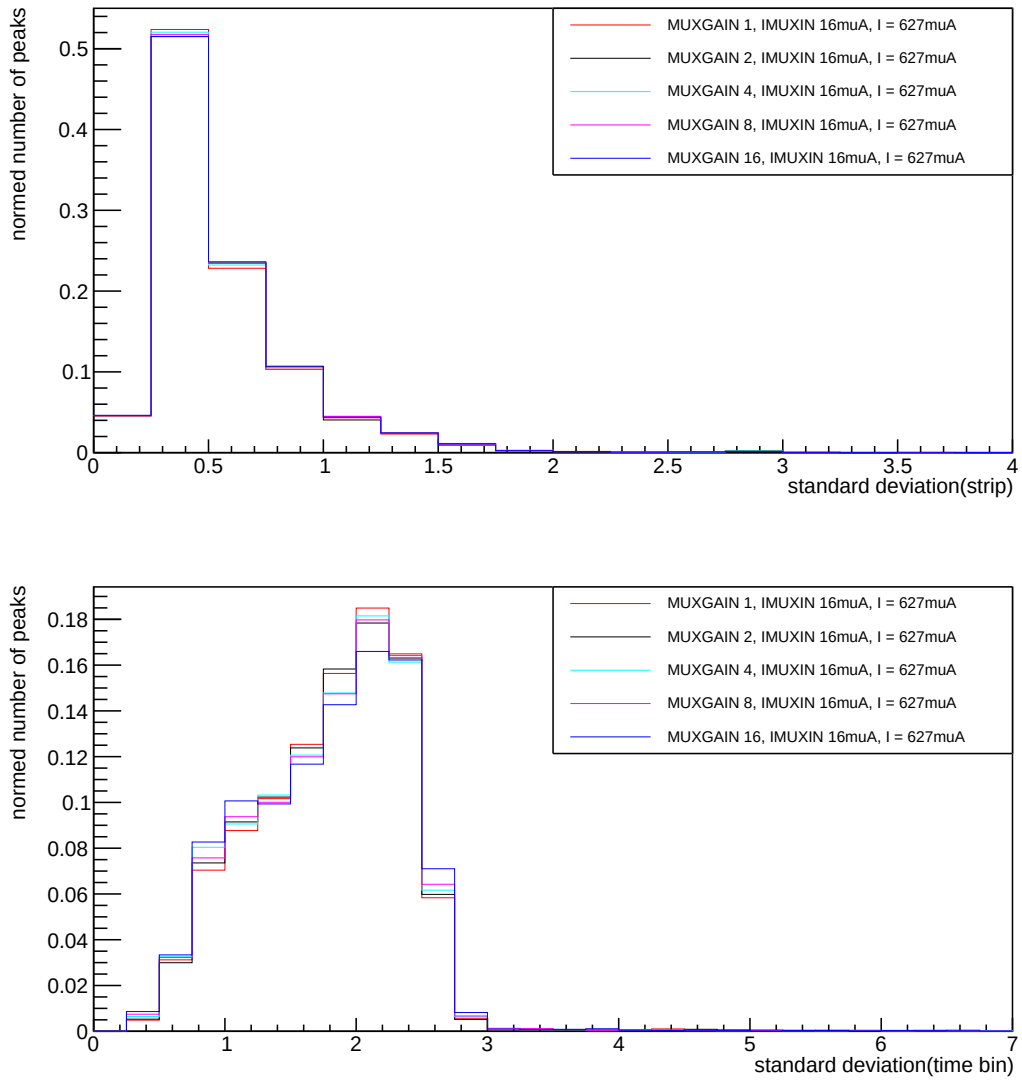

Figure 3.24: RMS of the width of a signal in number of signals is shown to strips (upper) and time bins (lower). Active X-ray source.

3.2.3 Baseline Shift

From the last paragraph one can draw the conclusion, that a better resolution of the temporal and spacial signal propagation can be reached by increase of the MUXGAIN. But higher MUXGAIN corresponds to a lower ADC count level of the baseline. To obtain a larger measuring range, i.e. larger signals without getting into the digital communication of the APVs, the position of the APV baseline can be manipulated. A possibility to move the level of the baseline is the change of the IMUXIN. Regarding to the analysis of the baseline position in ch. 3.2.1 the baseline should be moved for MUXGAIN 1 and 16 to a height of about 2800 ADC counts in average. A higher level is not possible, because the digital communication uses the ADC values smaller than 1100 ADC counts and larger than 3000 ADC counts. In fig. 3.25 the absolute ADC count is plotted against the strips. The mean and standard deviation is shown for each strip. One can see, that with an IMUXIN of 20 μA for MUXGAIN 1 and an IMUXIN of 60 μA for MUXGAIN 16 a baseline position of 2800 ADC counts can be reached. A detailed resolution of the data points is not necessary, because only the position of the baseline is of interest here.

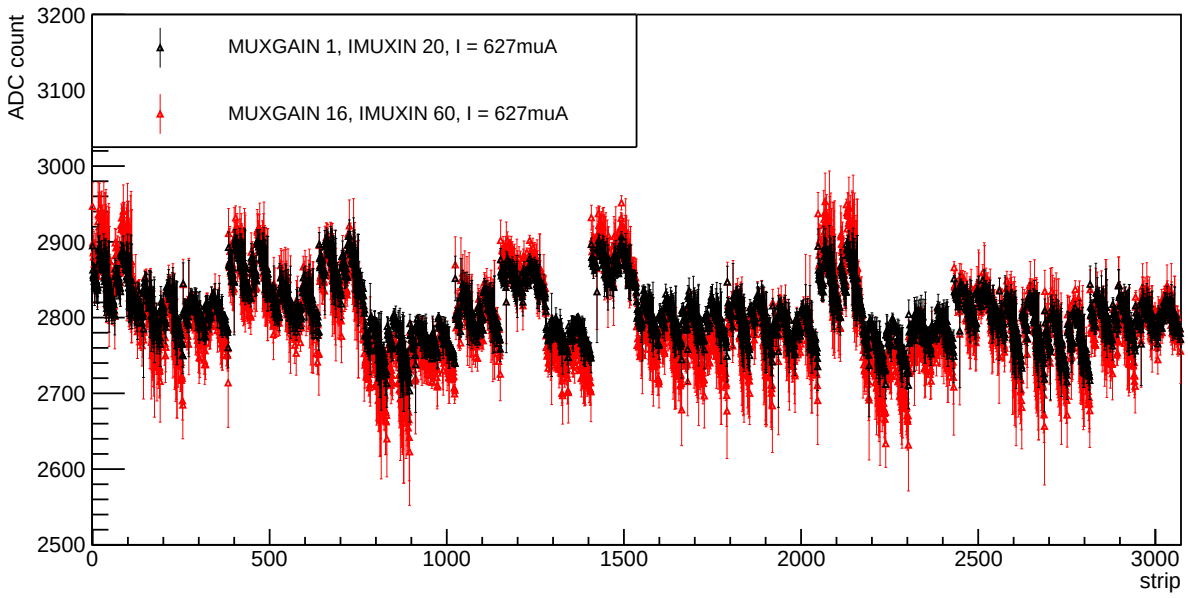

Figure 3.25: Mean of the ADC count for each strip and the corresponding standard deviation of baseline noise. The position of the baselines in the ADC count measured with different MUXGAINs. All strips (24 APVs) are shown.

3.3 Discussion

Taking all results into consideration , one can draw conclusions for the choice of the parameters current/HV, MUXGAIN and IMUXIN from the above measurements, in order to be able to measure the largest possible enhancement of the signals. The choice of operating voltage or current from 608 μA to 646 μA has mainly effects on the possible measuring accuracy. Nevertheless, the changes caused by change of the SRS gain in particular are in conflict with each other. The change of IMUXIN mainly influences the position of the baseline, less the propagation of the signals. These parameters are now discussed in detail.
Changes of the HV cause no change of the baseline position, but the noise level of the baseline increases (see fig. 3.11 and fig. 3.9). That means signals with low ADC count can hardly be distinguished from noise at higher voltages. The size of the signals is noticeably changed from 608 μA to 627 μA (see 3.4). This suggests taking measurements at a current of about 627 μA in order to evaluate signals in a good way.

This means that the possible analogue measurement range becomes smaller with simultaneously higher ADC counts of the signal peaks. However, the expansion of the peaks over time and space increases significantly at higher MUXGAIN, so that a larger part of the signals is above the noise and can be recorded (see fig. 3.24). Nevertheless the upper control plot in fig. 3.22 shows that a higher MUXGAIN causes a stronger noise of single strips, too. This results in more fake signals. By cutting signals with a to small spacial and temporal expansion and filtering some outstanding noisy APV-strip combination, the noise can be effectively reduced (see fig. 3.22). Therefore it makes sense not to measure with too high gain, since the analogue measuring range is significantly reduced. The remaining noisy strips must be evaluated separately, e.g. by a higher cut-off threshold for each strip. Completely filtering all the noisy strips could result in the loss of too many real signals.
The IMUXIN can change the position of the baseline. Together with a variation of the MUXGAIN it is a convenient tool, to allow for more precise measurements of the signal propagation.

In fig. 3.26 the temporal and spacial propagation of a single signal is shown. Time bins are plotted against strips with colour-coded ADC count.

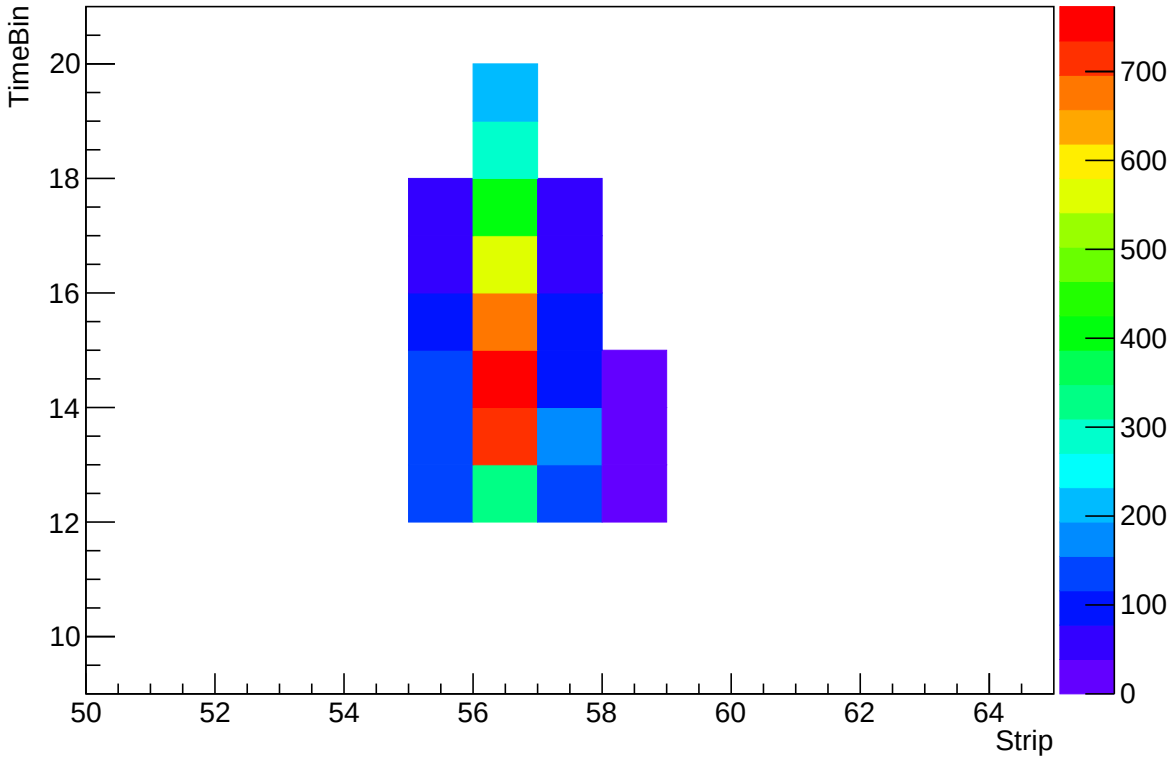

Figure 3.26: temporal (in time bins) and spatial (in strips) propagation of a single signal. The ADC count is colour-coded. The white area has ADC counts lower than the second threshold.

4 Summary and Conclusion

In this thesis the analysis of the temporal and spacial signal propagation in a triple GEM chamber is presented. The SR-System in raw data mode was used to record the measurements, so an ”unpacker” for the SRS data format has been programmed for the analysis.

The readout of a GEM chamber with the ”Raw data mode” of the SR-System was successful. When programming the ”unpacker”, the first aim was to separate the measured data from the different appended headers and header information. In particular, it had to be noted that for unknown reasons 1% of the data packages had not the expected length and so they could not be evaluated. After this unpacking of the raw data the focus was on distinguishing signals from noise. For this purpose a dynamic double-threshold peak finder and two filter stages were integrated into the program. So a multi purpose ”unpacker” for the SRS raw data readout was created successfully. It can be used also in other test stands or experiments using the set up consisting APVs, ADCs and FECs.

For the study of the signal propagation measurements with different parameters were performed. The operating voltage of the GEM chamber and the gain within the SRS were varied. It was found out, that a operating voltage of 3300 V (this corresponds to a current of 627 μA) is a good choice, because the noise, which suppresses lower signals, is reduced while the enhancement of the signals is scaled up. For the MUXGAIN and the IMUXIN a balance between signal amplification and the reduced measurement range had to be found. Benchmarks for the MUXGAIN are 8 and 16 with an IMUXIN of about 60 μA.

Based on this preliminary findings in the future one can investigate the signal distribution by analysing the resolution over the whole GEM chamber in more detail. Furthermore the benefit and impact of the IMUXIN can be studied by analysing the change of characteristic indicators for the signal propagation due to different IMUXIN values. Moreover the cause for the noisy channels can be analysed. So a better understanding of GEM chambers in combination with a SR-System can be achieved.

A Appendix

A.1 Appendix to ch. 2.3 Test Set up

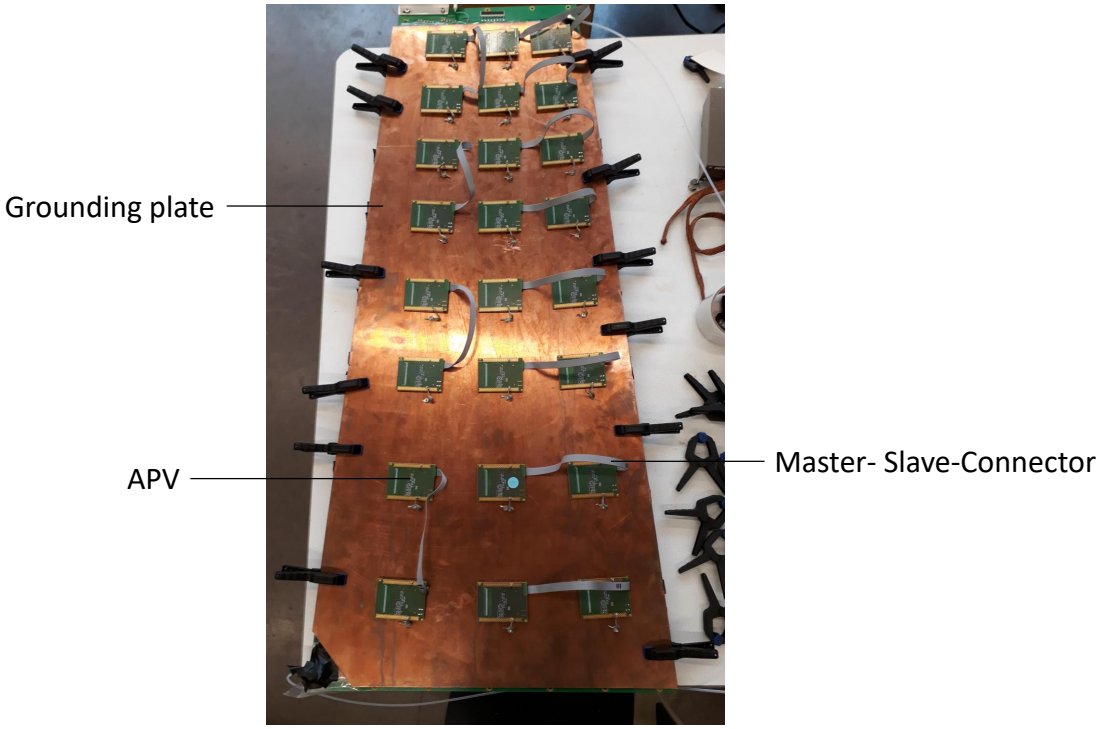

Figure A.1: Picture of the GEM chamber used for all measurements

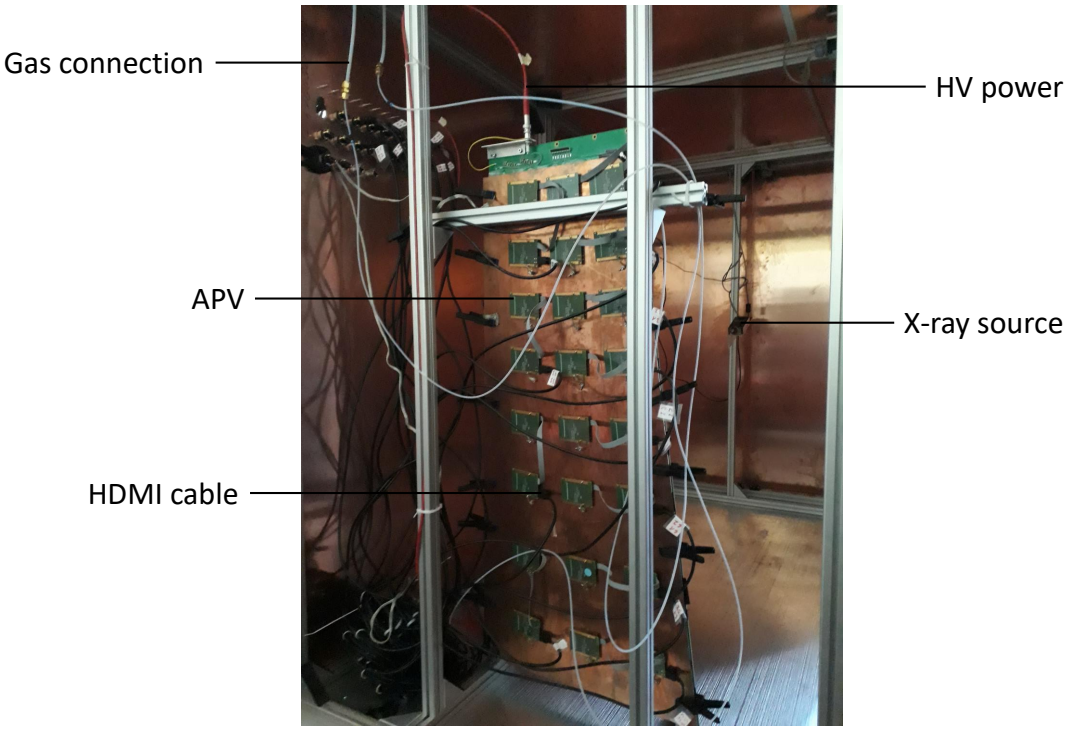

Figure A.2: Picture of the used GEM chamber placed in the copper box. In the background one can see the X-ray source.

A.2 Appendix to ch. 3.2.2 Variation of MUXGAIN and I/HV with X-ray

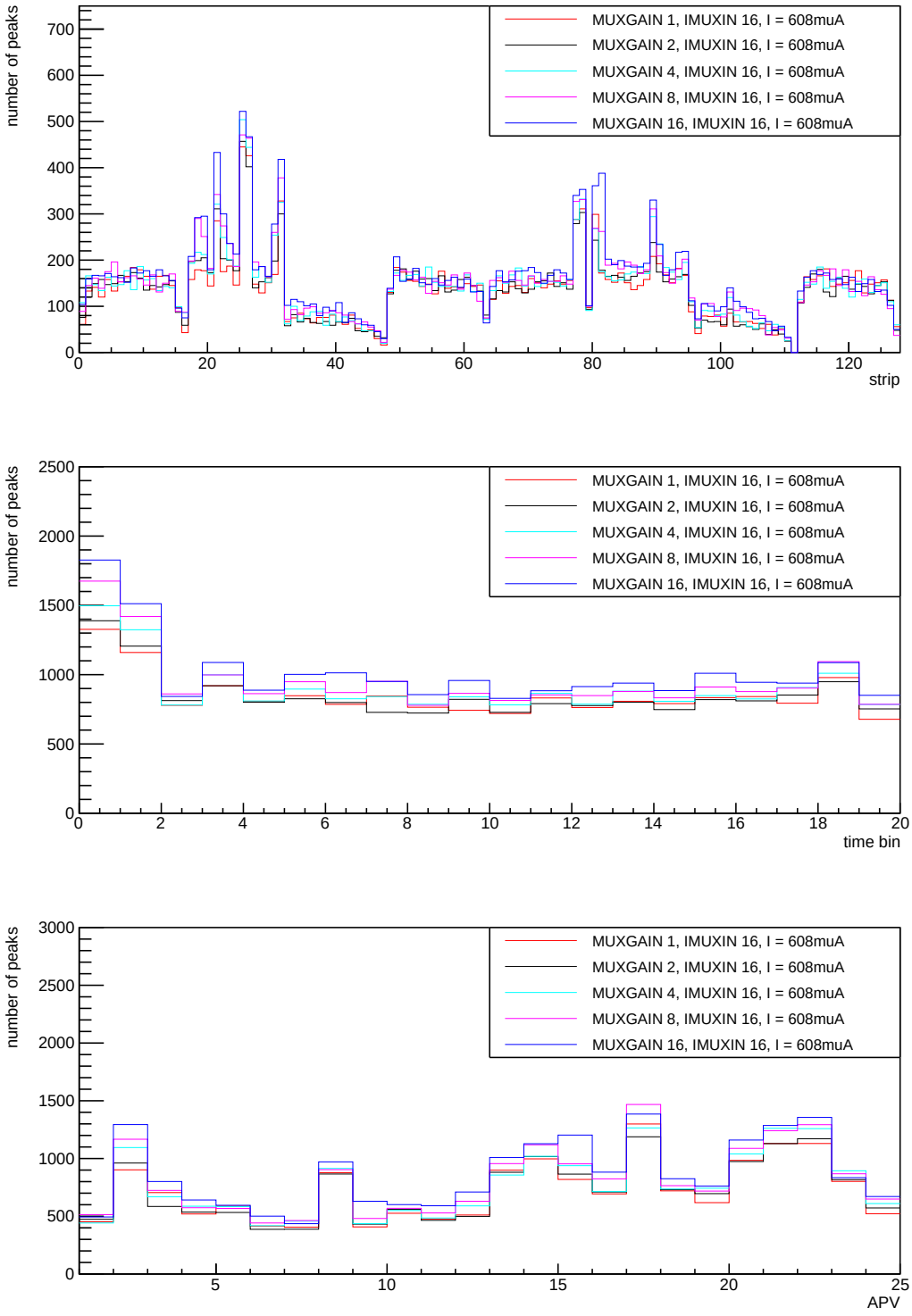

Figure A.3: Control plots filtered with stage 1 and 2; upper for the number of measured peaks plotted against the strips, middle for the number of measured signals plotted against the time bins, lower for the number of measured peaks plotted against the APV number. Active X-ray source..

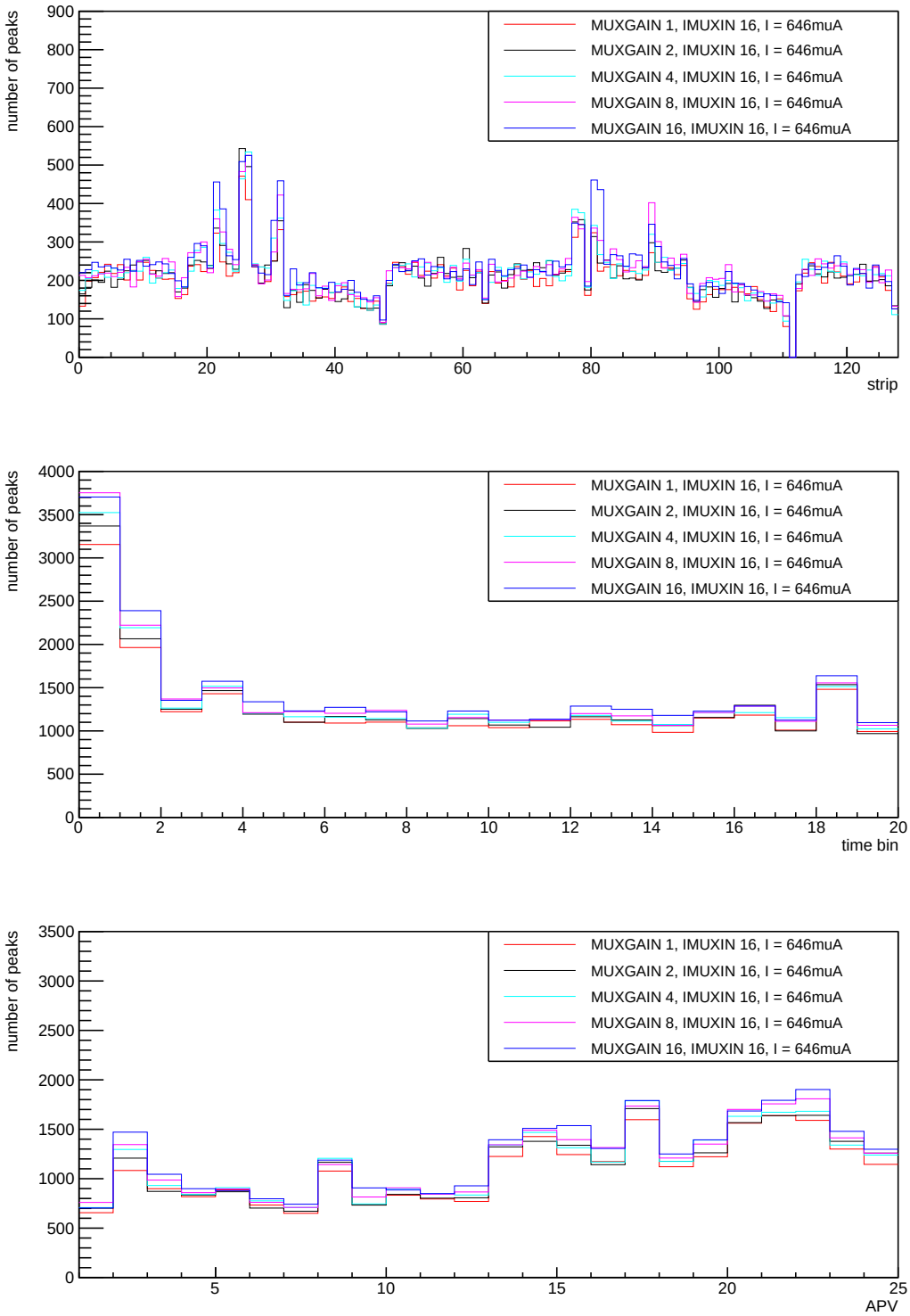

Figure A.4: Control plots filtered with stage 1 and 2; upper for the number of measured peaks plotted against the strips, middle for the number of measured signals plotted against the time bins, lower for the number of measured peaks plotted against the APV number. Active X-ray source.

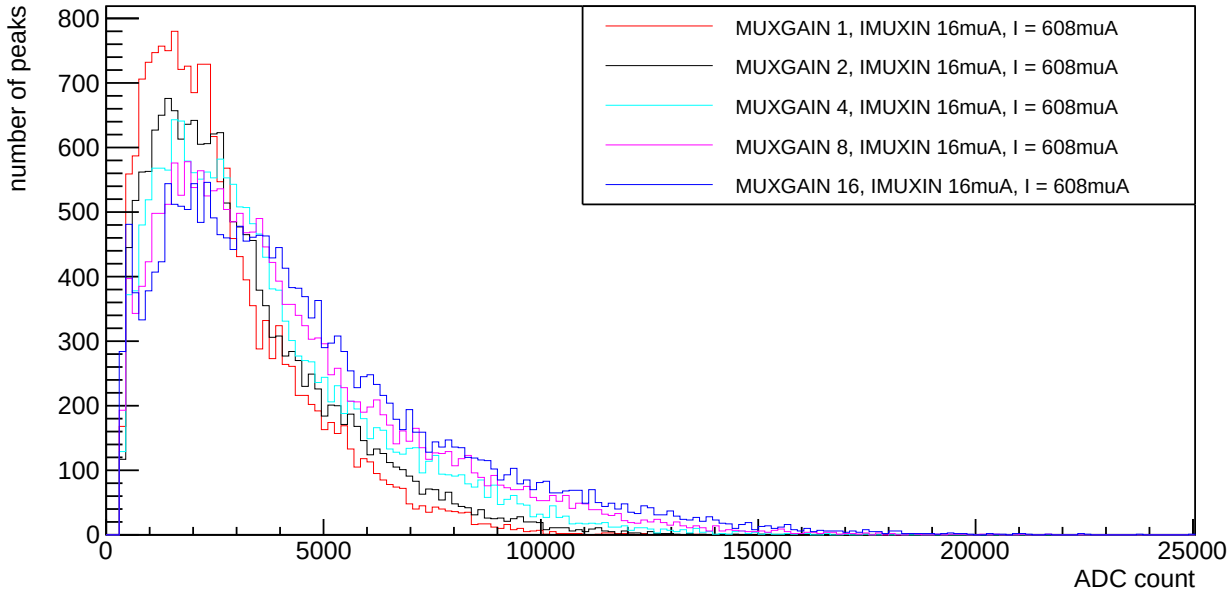

Figure A.5: Integral over the ADC count of the signals with filter stage 2 for different MUXGAINs. Active X-ray source.

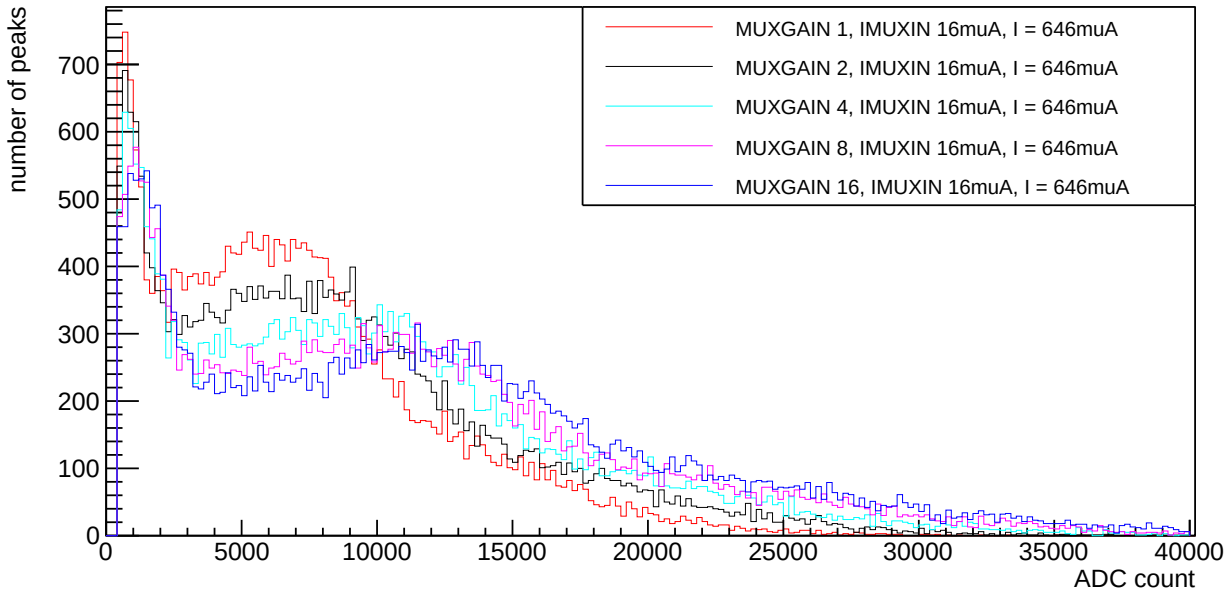

Figure A.6: Integral over the ADC count of the signals with filter stage 2 for different MUXGAINs. Active X-ray source.

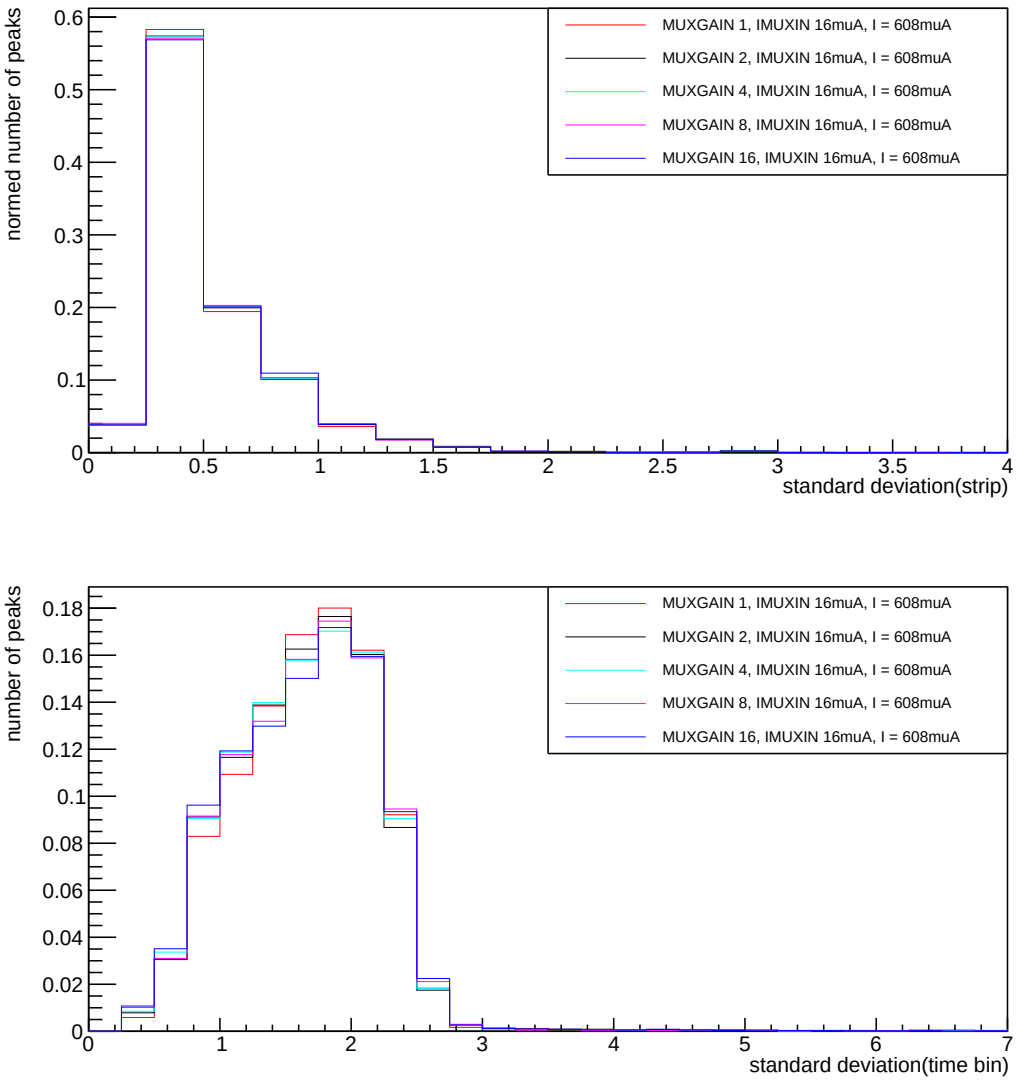

Figure A.7: Standard deviation of the width of a signal in number of signals is shown to strips (upper) and time bins (lower) for a current of 608 μA.

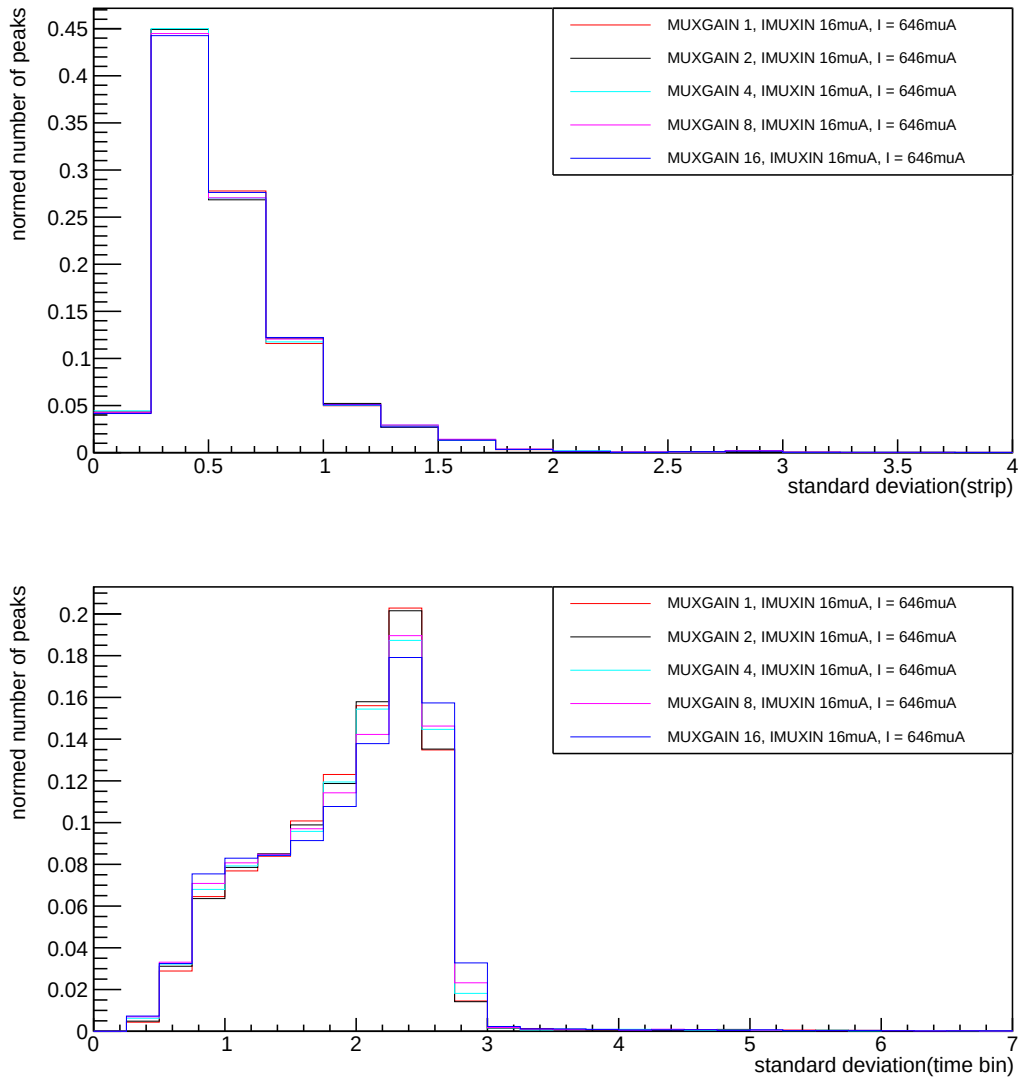

Figure A.8: Standard deviation of the width of a signal in number of signals is shown to strips (upper) and time bins (lower) for a current of 646 μA.

References

[1] Lawrence Jones (RAL). *APV25-S1 User GuideVersion 2.2*. URL: https://cds.cern.ch/record/1069892/files/cer-002725643.pdf.

[2] A. Sharma A. Colaleo A. Safonov and M. Tytgat. *CMS Technical Design Report for the Muon Endcap GEM Upgrade; CERN-LHCC-2015-012; CMS-TDR-013"*. Tech. rep. Sept. 2015. URL: https://cds.cern.ch/record/2021453?ln=de.

[3] CERN. *SRS Data Format*. URL: http://atlas.physics.arizona.edu/~kjohns/downloads/atlas-micromegas/srs-software-docs/SRS%20Data%20Format.pdf.

[4] CERN. *SRS Short User Guide*. URL: http://atlas.physics.arizona.edu/~kjohns/downloads/atlas-micromegas/srs-software-docs/SRS_Short_User_Guide.pdf.

[5] Italy Marco Villa from Desio. "Developing and evaluating new micropattern gas detectors". Dissertation. Rheinische Friedrich-Wilhelms-Universität Bonn. URL: http://d-nb.info/1052369855.

[6] L Shekhtman. "Micro-pattern gaseous detectors". In: *Nuclear Instruments and Methods in Physics Research Section A: Accelerators, Spectrometers, Detectors and Associated Equipment* 494.1 (2002). Proceedings of the 8th International Conference on Instrumentatio n for Colliding Beam Physics, pp. 128–141. ISSN: 0168-9002. DOI: 10.1016/S0168-9002(02)01456-0. URL: http://www.sciencedirect.com/science/article/pii/S0168900202014560.